

Compensating for source directivity in immersive wave experimentation

Xun Li, Johan Robertsson, Andrew Curtis, and Dirk-Jan van Manen

Citation: [The Journal of the Acoustical Society of America](#) **146**, 3141 (2019); doi: 10.1121/1.5131029

View online: <https://doi.org/10.1121/1.5131029>

View Table of Contents: <https://asa.scitation.org/toc/jas/146/5>

Published by the [Acoustical Society of America](#)



Compensating for source directivity in immersive wave experimentation

Xun Li,^{1,a)} Johan Robertsson,¹ Andrew Curtis,^{2,b)} and Dirk-Jan van Manen¹

¹Institute of Geophysics, ETH Zurich, Sonneggstrasse 5, 8092 Zurich, Switzerland

²School of GeoSciences, University of Edinburgh, James Hutton Road, Edinburgh EH9 3FE, United Kingdom

(Received 26 July 2019; revised 25 September 2019; accepted 8 October 2019; published online 6 November 2019)

A physical boundary mounted with active sources can cancel acoustic waves arriving at the boundary, and emit synthesized waves into the neighboring medium to fully control the acoustic wavefield in an experimental setup such as a water tank or air-filled cavity. Using the same principles, a physical experiment can be artificially immersed within an extended virtual (numerical) domain so that waves propagate seamlessly between the experimental setup and virtual domain. Such an immersive wave control experiment requires physical monopolar sources on the active boundary. However, real physical sources (e.g., piezoelectric transducers) project waves at middle-to-high sonic frequencies (e.g., 1–20 kHz) that do not fully conform to the theoretically required monopolar radiation pattern; if left uncorrected, this causes controlled wavefields to deviate from those desired in immersive experiments. A method is proposed to compensate for the non-monopole-like radiation patterns of the sources, and can be interpreted physically in terms of Huygens principle. The method is implemented as a pre-computation procedure that modifies the extrapolation Green's functions in the Kirchhoff-Helmholtz integral before the actual experiments take place. Two-dimensional finite-difference simulations show that the processing method can effectively suppress the undesired effect caused by non-monopolar active sources in immersive wave control experiments.

© 2019 Author(s). All article content, except where otherwise noted, is licensed under a Creative Commons Attribution (CC BY) license (<http://creativecommons.org/licenses/by/4.0/>).

<https://doi.org/10.1121/1.5131029>

[JC]

Pages: 3141–3158

I. INTRODUCTION

By emitting carefully chosen signals, acoustic sources (e.g., loudspeakers) can be used as acoustic sinks. By spanning physical boundaries with arrays of sinks, that boundary may be rendered acoustically transparent (Olson, 1956; Orduña Bustamante and Nelson, 1992; Williams, 1984); thus, for example, the boundary of an anechoic chamber can cancel undesired sound (Beyene and Burdisso, 1997; Guicking and Karcher, 1984; Smith *et al.*, 1999). In addition, active sources surrounding an experiment can mimic or produce sound wavefields to create an artificial immersive environment within which one hears sounds apparently arriving from various directions or locations (e.g., Berkhout *et al.*, 1993; Camras, 1968; Nelson, 1994). Such experiments control acoustic wavefields in an interior domain, but an active boundary mounted with densely spaced acoustic sources can also be used to control the wavefield in an exterior domain such that from the outside the interior domain appears to be acoustically transparent (also known as cloaking) or appears to contain objects which do not physically exist in the interior domain (holography) (Miller, 2006; van Manen *et al.*, 2015; Vasquez *et al.*, 2011).

Designs of active boundaries for wavefield cancellation and production using dense source arrays physically

originate from Huygens principle; a wavefield can be represented as monopolar isotropic secondary sources distributed continuously along each wavefront if the wavefront coincides with a rigid boundary such that dipolar sources are not involved (Baker and Copson, 1950; Miller, 1991). However, physical sources on an active boundary almost never exhibit isotropic radiation patterns as these are difficult and hence expensive to engineer in a laboratory (Ise, 1999; Willard, 2019; Willard *et al.*, 2018). For this reason, wavefield cancellation and production are always imperfect, even if exactly correct wave signals for emission at the active boundary are known.

Vasmel *et al.* (2013) proposed an active boundary design that can exactly build an immersive experimental environment where waves that should enter the physical domain are produced, and waves leaving the experimental domain are canceled at the surrounded active boundary. The design of the active boundary is based on immersive or exact boundary condition theory (Givoli and Cohen, 1995; Ting and Miksis, 1986; van Manen *et al.*, 2007), which is inherently obtained using an acoustic representation theorem (Aki and Richards, 2002) and a Kirchhoff-Helmholtz integral (e.g., Wapenaar, 1993). In addition to achieving exact wavefield cancellation at the active boundary surrounding a physical domain, van Manen *et al.* (2007) and Vasmel *et al.* (2013) proposed the concept of a (numerical) virtual domain within which the physical experimental setup can be fully immersed such that waves travel seamlessly back and forth

^{a)}Electronic mail: xun.li@erdw.ethz.ch

^{b)}Also at: Institute of Geophysics, ETH Zurich, Zurich, Switzerland.

between the physical and virtual domains. The immersive experimentation setup is depicted in Fig. 1(a). It involves (1) physically recording wavefield quantities (i.e., pressures and particle velocities) at the recording surface S^{rec} , (2) Kirchhoff-Helmholtz extrapolation of the wavefield from S^{rec} to each source on the active boundary S^{src} that is computed numerically in real time during the experiment, and (3) physically injecting waves at the active source boundary S^{src} based on the extrapolated quantities and a numerical simulation of the virtual medium that may contain arbitrary objects or properties. Waves injected at the active boundary S^{src} in the laboratory are thus calculated from both physical measurements and numerical simulations. In Fig. 1(a), out-going waves traveling from the physical domain to the virtual domain (ray path 1) and the associated reflected waves at the rigid boundary (ray path 3) are canceled while in-going waves coming from the virtual domain [ray path 2 in Fig. 1(b)] are produced inside the physical domain (ray path 4). In this case, a physical domain shown in Fig. 1(a) can be fully immersed into a surrounding virtual domain, achieving the kinematic and dynamic illusion within the physical domain that all waves propagate in the combined physical and virtual domain, namely, the full domain shown in Fig. 1(b). Acoustic immersive experimentation theory for the active source boundary involves a rigid boundary that contains densely spaced active sources and encloses an experimental setup (Vasmel et al., 2013), or other boundary

types can be used such as a free surface (Broggini et al., 2017).

An acoustic immersive wave control experiment can be simulated using numerical finite-difference modeling to machine-precision of the result where a simulated physical domain is perfectly immersed into a virtual domain (Broggini et al., 2017; Vasmel et al., 2013). Becker et al. (2018) and Börsing et al. (2019) conducted pioneering one-dimensional (1D) immersive wave experiments that demonstrated physical immersion, cloaking, and holography in a physical laboratory. However, these works are achieved in 1D experiments where sources (moving coil loudspeakers) radiate in only a single direction. For 2D and 3D immersive wave control experimentation, physical sources mounted on the rigid boundary should be monopoles, as this is also required in other types of active boundary designs and sound field control experiments (Berkhout et al., 1993; Ise, 1999; Miller, 2006). The moving coil loudspeakers used in 1D immersive wave experiments (Becker et al., 2018), for instance, do not behave like a monopole. The other choice could be piezoelectric sources. Although piezoelectric technology facilitates the development of transducers with broad operating frequency bands and small sizes (Sherman and Butler, 2007; Wilson, 1988; Wilson and McMahon, 1987), the manufacture of a physical monopolar source with a wide-aperture emittance and broadband (low) frequency range (1–20 kHz) is still difficult and expensive since it

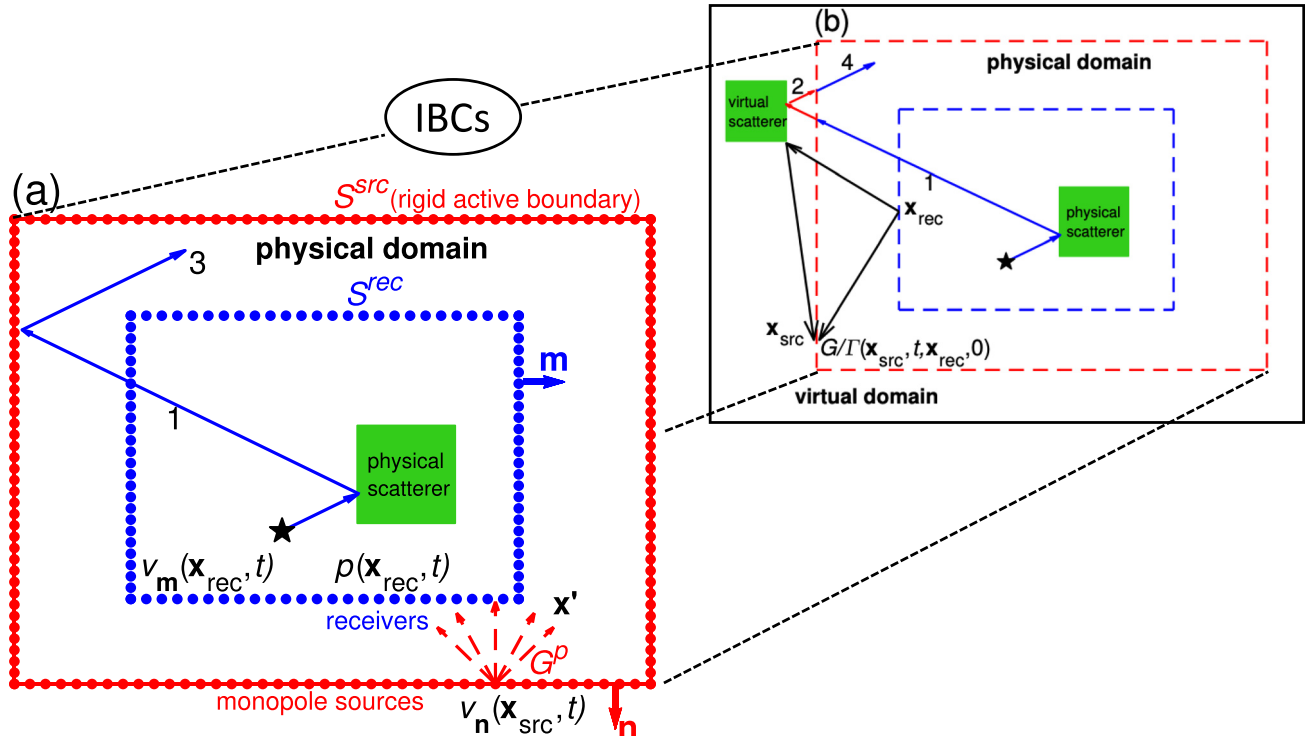


FIG. 1. (Color online) Schematic plot of (a) immersive wave control experimentation in two-dimensions and (b) an immersive environment where the physical domain is immersed into the virtual domain using immersive boundary conditions (IBCs). (a) The experimentation includes a recording surface S^{rec} (with normal \mathbf{m}) spanned by closely spaced receivers (blue dots), an active boundary S^{src} (the red rectangle with normal \mathbf{n}) co-located with the rigid boundary (“rigid active boundary”) mounted with closely spaced sources (red dots). The black star denotes an internal source that generates wavefield energy. The Green’s function G^p is denoted for waves (dashed red arrows) propagating from monopolar sources deployed on the active boundaries with $v_n(\mathbf{x}_{src}, t)$ as source signatures [see Eq. (1)], and \mathbf{x}' denotes an arbitrary point. (b) The dashed red and blue lines denote the location of active boundary S^{src} and S^{rec} , and the solid black arrow denotes the computed Green’s functions G and Γ between receivers at \mathbf{x}_{rec} on S^{rec} and sources at \mathbf{x}_{src} on S^{src} . (a, b) Arrows 1 to 4 represent paths of energy propagation in the physical (blue) and virtual (red) domains.

requires a spherical-structural design for piezoelectric elements (Willard, 2019; Willard *et al.*, 2018). Cost-effective piezoelectric source designs such as the Bender Mode X-Spring (Woollett and Finch, 1990) or Tonpilz transducer (Wilson, 1988) with a non-spherical piezoelectric structure cannot satisfy the monopolar-source requirement for the active boundary in immersive wave control experiments (Willard, 2019), so that physical sources have anisotropic radiation patterns in wave control experiments (Ebrom and McDonald, 1994). In this paper, we use accurate simulations to demonstrate the effects of using realistic sources with non-monopolar radiation patterns in 2D immersive experimentation, and introduce a method that compensates for non-ideal radiation patterns in real time in physical experiments. The method will contribute to the accuracy of many 2D and 3D applications involving active boundaries comprising real sources such as those in Berkhouit *et al.* (1993), Coleman *et al.* (2014), and Kirkeby and Nelson (1993), and can be generalized to correct other types of physical waves.

In Sec. II we review the acoustic immersive boundary condition theory and incorporate new wavefield processing methods that compensate for non-monopole-like radiation patterns of physical sources on an active boundary. In Sec. III, we demonstrate the significance of non-monopole-like radiation on (immersive) wave control experimentation and the proposed compensation method. In Sec. IV, we discuss (1) the case where radiation pattern varies from source to source on the active boundary, (2) physical insights into the compensation method, and (3) implications for active boundaries in applications such as audio control systems (Cai *et al.*, 2014), noise minimization (Olson, 1956), and cloaking (van Manen *et al.*, 2015; Miller, 2006). Section V summarizes our conclusion.

II. THEORY

We consider an acoustic experimental setup such as a water tank or air-filled room/cavity surrounded by an active rigid boundary mounted with acoustic transducers. Cancellation of out-going waves that arrive at the boundary and synthesis of in-going waves arriving from the external virtual domain are exactly achieved by an immersive boundary condition (IBC) derived from a wavefield reciprocity relation (Broggini *et al.*, 2017; van Manen *et al.*, 2007; Vasmel *et al.*, 2013), which produces the wavefield

$$P^{IBC}(\mathbf{x}', t) = - \int_{S^{src}} G^p(\mathbf{x}', t, \mathbf{x}_{src}, 0) * v_{\mathbf{n}}(\mathbf{x}_{src}, t) dS. \quad (1)$$

Here, $G^p(\mathbf{x}', t, \mathbf{x}_{src}, 0)$ is the Green's function involving a monopolar pressure source at \mathbf{x}_{src} and a pressure response at an arbitrary (observation) point \mathbf{x}' inside the physical domain with a rigid boundary. One can interpret the right hand side of Eq. (1) as a superposition (integration) of monopolar pressure sources mounted continuously at points \mathbf{x}_{src} distributed around the inside of a rigid outer boundary of an interior domain (Vasmel *et al.*, 2013), emitting energy in the inward-normal direction $-\mathbf{n}$. Green's functions $G^p(\mathbf{x}', t, \mathbf{x}_{src}, 0)$ then represent the wave propagation to point \mathbf{x}' that would be

observed in the physical medium if an impulsive monopolar source had been fired at \mathbf{x}_{src} . The time signatures for the boundary sources at \mathbf{x}_{src} are the normal particle velocities $v_{\mathbf{n}}(\mathbf{x}_{src}, t)$ of all waves arriving at the active source boundary S^{src} : these include out-going waves from the interior physical domain [ray path 1 in Figs. 1(a)] and in-going waves from the exterior (numerical) virtual domain (ray path 2). Provided that one knows the normal particle velocities $v_{\mathbf{n}}(\mathbf{x}_{src}, t)$ for both the in-going and out-going waves when they arrive at boundary S^{src} , the active boundary with the emitted wavefield P^{IBC} in Eq. (1) cancels (reflections from) out-going waves [ray path 3 in Fig. 1(a)] and produces desired in-going waves (ray path 4) in immersive wave control experiments (Broggini *et al.*, 2017; Vasmel *et al.*, 2013).

In the laboratory, the active source boundary S^{src} is also the rigid boundary of the experimental setup, as shown in Fig. 1(a). The normal particle velocity for the out-going waves [ray path 1 in Fig. 1(a)] at a rigid source boundary is always zero by definition of the boundary condition and so cannot be physically measured in the laboratory using receivers deployed on S^{src} . An alternative solution involves recording the waves over an interior recording surface S^{rec} in the experimental setup and extrapolating that wavefield to \mathbf{x}_{src} using the Kirchhoff-Helmholtz integral to calculate the normal particle velocities $v_{\mathbf{n}}(\mathbf{x}_{src}, t)$ required by Eq. (1) (Miller, 2006; van Manen *et al.*, 2007):

$$v_{\mathbf{n}}(\mathbf{x}_{src}, t) = \int_{S^{rec}} [G(\mathbf{x}_{src}, t, \mathbf{x}_{rec}, 0) * v_{\mathbf{m}}(\mathbf{x}_{rec}, t) + \Gamma(\mathbf{x}_{src}, t, \mathbf{x}_{rec}, 0) * p(\mathbf{x}_{rec}, t)] \cdot \mathbf{m} dS, \quad (2)$$

where $G(\mathbf{x}_{src}, t, \mathbf{x}_{rec}, 0)$ and $\Gamma(\mathbf{x}_{src}, t, \mathbf{x}_{rec}, 0)$ are the Green's functions representing the normal (\mathbf{n}) particle velocity responses at \mathbf{x}_{src} due to (for G) impulsive monopolar pressure sources located at \mathbf{x}_{rec} and (for Γ) impulsive point sources of body force located at \mathbf{x}_{rec} with force direction \mathbf{m} normal to the recording surface S^{rec} , respectively. The point source of body force can be regarded as a dipole source (Becker *et al.*, 2018; Broggini *et al.*, 2017; Vasmel *et al.*, 2013). In this paper, the asterisk refers to convolution in time t . The numerically modeled medium [Fig. 1(b)] used to compute the Green's functions in Eq. (2) must include the virtual domain and the space between the recording surface S^{rec} and active boundary S^{src} . In this case, the physical structure of the space between S^{rec} and S^{src} in the laboratory [see Fig. 1(b)] must be precisely known and replicated in the numerically modeled medium. This space can be often treated homogeneous in an experimental setup such as a water tank Vasmel *et al.* (2013). The physical medium inside S^{rec} is irrelevant to Kirchhoff-Helmholtz extrapolation [Eq. (2)] and in fact can be set arbitrarily when computing the Green's functions (Broggini *et al.*, 2017; Thomson, 2012). Velocities $v_{\mathbf{n}}$ from Eq. (2) then include contributions from all in-going and out-going waves from both physical and virtual domains as required for Eq. (1). Figure 1 includes the physical quantities involved in Eq. (2). The active source boundary S^{src} is equivalent to the “emitting surface” referred to in Broggini *et al.* (2017) and Vasmel *et al.* (2013).

Experimentation involving an active source boundary based on Eqs. (1) and (2) can fully immerse a physical experiment into a virtual domain (van Manen *et al.*, 2007; Vasmel *et al.*, 2013). In a laboratory experiment, receivers on the recording surface S^{rec} record particle velocities $v_{\mathbf{m}}(\mathbf{x}_{rec}, t)$ in the normal direction \mathbf{m} to S^{rec} and pressure $p(\mathbf{x}_{rec}, t)$ of propagating waves, and sources on S^{src} emit time series $v_{\mathbf{n}}(\mathbf{x}_{src}, t)$. Since extrapolated particle velocities $v_{\mathbf{n}}(\mathbf{x}_{src}, t)$ account for both out-going and in-going waves (ray paths 1 and 4 in Fig. 1), one does not need to measure or compute the particle velocities at the active source boundary S^{src} for out-going and in-going waves separately (Broggini *et al.*, 2017). Green's functions G and Γ in Eq. (2) are pre-computed in a virtual numerical domain before immersive experiments take place [solid black rays in Fig. 1(b)]. The Green's functions G and Γ describe the propagation of wave energy from the recording wavefront at S^{rec} to the active boundary S^{src} where arriving waves computed and predicted using Eq. (2) can be out-going or in-going. In-going waves are produced using sources mounted at the rigid boundary when the waves cross the active source surface S^{src} [ray path 4 in Fig. 1(b)]. During an immersive experiment, Kirchhoff-Helmholtz extrapolation is computed numerically in real time, while the physical acoustic experiment continues in the interior domain. Provided that particle velocities $v_{\mathbf{n}}(\mathbf{x}_{src}, t)$ are computed numerically from Eq. (2) before out-going waves [ray path 1 in Fig. 1(a)] physically arrive at the active surface S^{src} at some future time t , active sources on the rigid boundary of the experimental setup can project wavefield P^{IBC} by emitting the computed particle velocities $v_{\mathbf{n}}(\mathbf{x}_{src}, t)$ to cancel those out-going waves. Hence Kirchhoff-Helmholtz extrapolation must predict and project those wavefield quantities in less time than it takes the waves to physically propagate from the recording surface S^{rec} to the active boundary S^{src} . This real-time computation can be achieved using a high-performance computing and control unit [e.g., a field-programmable gate array (FPGA)] (Becker *et al.*, 2018).

A physical source with a non-monopole-like radiation pattern does not satisfy the theoretical assumption made in Eq. (1), that G^p represents physical wave propagation from the active boundary distributed with monopoles in the laboratory. In immersive wave control experiments with non-monopole-like sources, the emitted wavefield in Eq. (1) becomes

$$\tilde{P}^{IBC}(\mathbf{x}', t) = - \int_{S^{src}} \tilde{G}^p(\mathbf{x}', t, \mathbf{x}_{src}, 0) * v_{\mathbf{n}}(\mathbf{x}_{src}, t) dS, \quad (3)$$

where $v_{\mathbf{n}}(\mathbf{x}_{src}, t)$ follows Eq. (2), and \tilde{G}^p is a Green's function from a non-monopolar source which is the imperfect counterpart of G^p in Eq. (1).

The radiation pattern of a physical source can be measured at radius R using the geometry shown in Fig. 2. We denote the acoustic radiation measurement of an ideal monopolar source and a physical source mounted on a rigid boundary by $M^p(\theta, t)$ and $\tilde{M}^p(\theta, t)$, respectively. These represent impulsive pressure responses measured in every direction θ in a homogeneous (half-)free space. Here the 2D

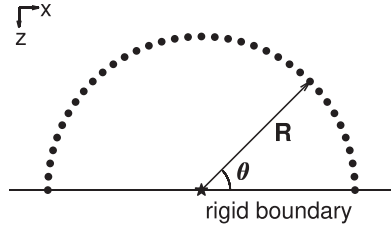


FIG. 2. Geometry used to measure the directivity or radiation pattern of a physical source. The star denotes the source mounted on a rigid boundary. Angle θ is the relative orientation of receivers (dots) with respect to the mounted physical source on the rigid boundary, and R is the radius of the semi-circular acquisition geometry.

parametrization of the source radiation pattern neglects the horizontal directivity of the source, which varies with azimuth and is commonly small compared to the directivity varying with vertical angles for piezoelectric transducers (Willard, 2019; Willard *et al.*, 2018). The horizontal directivity can be taken into account with a generalized 3D compensation method based on the same idea.

We define directive filters $W(\theta, t)$ to be matched filters between the impulsive responses of a physical source $\tilde{M}^p(\theta, t)$ and a monopolar source $M^p(\theta, t)$ in each direction θ :

$$M^p(\theta, t) = \tilde{M}^p(\theta, t) * W(\theta, t). \quad (4)$$

Directive matched filterers can be computed from recordings of $\tilde{M}^p(\theta, t)$ and the ideal response $M^p(\theta, t)$, using a temporal-frequency domain water-level deconvolution scheme (Press *et al.*, 2007). The deconvolution is carried out separately for each direction θ . A non-monopole-like radiation pattern can then be compensated in direction θ using the corresponding matched filter $W(\theta, t)$ in Eq. (4).

Assume for the moment that all active sources mounted on the rigid boundary have the same radiation pattern. While such an assumption is not required by the method, it simplifies the derivation; the extension to the case where radiation patterns vary from source to source is presented in Sec. IV. The algorithm is described for a 2D immersive wave control experiment, but 3D experiments may be treated similarly with sources having radiation patterns that vary with azimuth and incidence angle.

The pre-computed Green's functions $G(\mathbf{x}_{src}, t, \mathbf{x}_{rec}, 0)$ and $\Gamma(\mathbf{x}_{src}, t, \mathbf{x}_{rec}, 0)$ in Eq. (2) implicitly contain information about the direction of propagation when waves arrive at the active source boundary S^{src} , which can be analyzed in the frequency-wavenumber (f-k) domain. We apply a 2D frequency-wavenumber Fourier transform to the Green's functions G and Γ (Yilmaz, 2001) along the time axis t and the active source boundary \mathbf{x}_{src} for each receiver \mathbf{x}_{rec} to obtain

$$\hat{G}(k, f, \mathbf{x}_{rec}) = \int_t \int_{x_{src}} G(\mathbf{x}_{src}, t, \mathbf{x}_{rec}, 0) e^{-i2\pi ft} e^{i2\pi kx_{src}} dx dt \quad (5)$$

and

$$\hat{\Gamma}(k, f, \mathbf{x}_{rec}) = \int_t \int_{x_{src}} \Gamma(\mathbf{x}_{src}, t, \mathbf{x}_{rec}, 0) e^{-i2\pi ft} e^{i2\pi kx_{src}} dx dt, \quad (6)$$

where the spatial axis \mathbf{x}_{src} can be treated as four separate lines forming the closed rectangle in a 2D immersive wave control experiment depicted in Fig. 1, where the boundary sources mounted in the inwards-normal direction ($-\mathbf{n}$) to the active boundary S^{src} are shown in Fig. 3. Note that in Eqs. (5) and (6) the symbol $\hat{\cdot}$ in $\hat{G}(k, f, \mathbf{x}_{rec})$ and $\hat{\Gamma}(k, f, \mathbf{x}_{rec})$ denotes the equivalent counterparts in the f-k domain, whereas below we use $\hat{\cdot}$ in $\hat{W}(\theta, f)$ to denote the frequency domain counterpart of $W(\theta, t)$ in Eq. (4); the arguments define which Fourier transform has been applied in each case. As illustrated in Fig. 3, angle θ in Fig. 2 can be related to the wave propagation direction $\alpha = c_0 k / f$ in the f-k domain,

$$\theta = \pi/2 + \arcsin(c_0 k / f), \quad (7)$$

where $-1 < c_0 k / f < 1$ and c_0 is the local acoustic velocity at \mathbf{x}_{src} .

The directive matched filter can be used to compensate for the non-monopole-like radiation pattern of a physical source in any direction when the filter is convolved with the source signature as in Eq. (4). Instead of associating the filters with the source signature $v_{\mathbf{n}}(\mathbf{x}_{src}, t)$ in Eq. (1), one can incorporate filters $\hat{W}(\theta, f)$ into the pre-computed Green's functions $G(\mathbf{x}_{src}, t, \mathbf{x}_{rec}, 0)$ and $\Gamma(\mathbf{x}_{src}, t, \mathbf{x}_{rec}, 0)$ in Eq. (2). In the f-k domain, this association involves the counterpart Green's functions in Eqs. (5) and (6) and can be expressed as

$$\hat{G}(k, f, \mathbf{x}_{rec}) = \hat{G}(k, f, \mathbf{x}_{rec}) \hat{W}(\pi - \theta, f) \quad (8)$$

and

$$\hat{\Gamma}(k, f, \mathbf{x}_{rec}) = \hat{\Gamma}(k, f, \mathbf{x}_{rec}) \hat{W}(\pi - \theta, f), \quad (9)$$

where multiplication in the frequency domain is equivalent to convolution in the time domain, θ can be expressed by

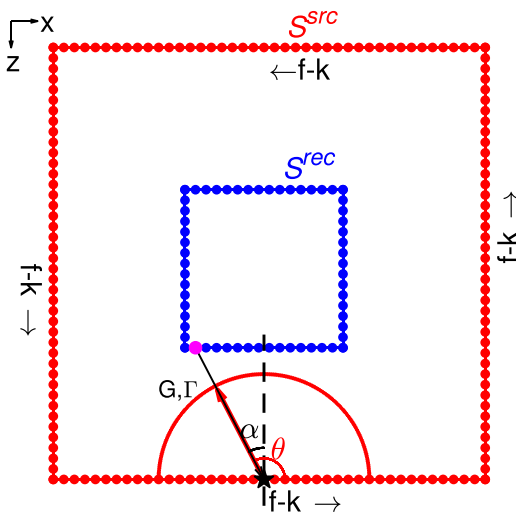


FIG. 3. (Color online) Schematic plot of the angle relationship in the f-k processing method. For each receiver (e.g., the magenta dot) at the recording surface S^{rec} , the Greens functions G and Γ are f-k transformed along the time axis and the four sides of the source boundary S^{src} . Angle α denotes a wave propagation direction, and angle θ denotes the source directivity for the source located at the black star.

Eq. (7) in the f-k domain, and $\pi - \theta$ is used as the argument of \hat{W} so that the non-monopolar radiation pattern in the direction of reflection at the active source boundary S^{src} for outgoing waves [ray path 3 in Fig. 1(a)] is compensated, as are waves entering the domain at the same angle (ray path 4). Note that Eqs. (8) and (9) work equally well for in-going and out-going waves, as indicated in Fig. 4. In the f-k domain, a pair of in-going and out-going waves shown in Fig. 4 share the same value of f/k . For the out-going waves with incident angle α , one compensates for the non-monopolar radiation pattern at the reflected angle $-\alpha$ (i.e., $\pi - \theta$) since we wish to cancel the reflection. For the in-going waves, one compensates in the propagation direction $-\alpha$. Thus, the cancellation and production of out-going waves and in-going waves, respectively, share the same directive matched filters at each compensation direction; one therefore does not need to process the Green's functions for in-going and out-going waves separately.

The processed Green's functions \tilde{G} and $\tilde{\Gamma}$ are inverse f-k Fourier transformed back to the spatial-temporal domain, resulting in $\tilde{G}(\mathbf{x}_{src}, t, \mathbf{x}_{rec}, 0)$ and $\tilde{\Gamma}(\mathbf{x}_{src}, t, \mathbf{x}_{rec}, 0)$ which can be applied in immersive wave control experimentation so that Eqs. (1) and (2) become

$$P_{comp}^{IBC}(\mathbf{x}', t) = - \int_{S^{src}} \tilde{G}^p(\mathbf{x}', t, \mathbf{x}_{src}, 0) * \tilde{v}_{\mathbf{n}}(\mathbf{x}_{src}, t) dS \quad (10)$$

and

$$\begin{aligned} \tilde{v}_{\mathbf{n}}(\mathbf{x}_{src}, t) = & \int_{S^{rec}} [\tilde{G}(\mathbf{x}_{src}, t, \mathbf{x}_{rec}, 0) * v_{\mathbf{m}}(\mathbf{x}_{rec}, t) \\ & + \tilde{\Gamma}(\mathbf{x}_{src}, t, \mathbf{x}_{rec}, 0) * p(\mathbf{x}_{rec}, t)] \cdot \mathbf{m} dS, \end{aligned} \quad (11)$$

where quantities without a tilde are identical to those in Eqs. (1) and (2), and \tilde{G}^p represents the Green's function from a non-monopole-like source as in Eq. (3). The compensation of the non-monopolar radiation pattern actually applies to the compensated extrapolated particle velocities $\tilde{v}_{\mathbf{n}}(\mathbf{x}_{src}, t)$ in Eq. (10) by associating the directive matched filters with the pre-computed Green's functions in Eq. (2). Particle

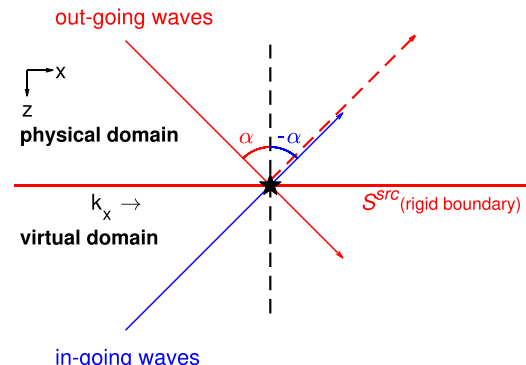


FIG. 4. (Color online) Schematic interpretation of the f-k processing scheme that works for both the out-going waves (the solid red arrow) propagating from the physical domain to the virtual domain, and in-going waves (the blue arrow) propagating from the virtual domain to the physical domain. The dashed red arrow denotes the undesired reflected waves that will be present if the active sources (the black star) are not deployed on the rigid boundary.

velocities $\tilde{v}_n(\mathbf{x}_{src}, t)$ compensate for the non-monopolar radiation pattern within \tilde{G}^P for the emitting wavefield P_{comp}^{IBC} , canceling and producing waves at the active source boundary S^{src} in all directions. Finally the required f-k processing is all carried out prior to conducting immersive wave control experiments, and hence does not lead to an increase in the cost of the real-time computation [i.e., Eqs. (2) and (11)].

The Green's functions in Eq. (2) are computed in the virtual medium by putting a source (monopole or dipole) at the recording surface S^{rec} and recording around the active source boundary S^{src} (see also Broggini *et al.*, 2017) without the rigid boundary applied. The source at the recording surface S^{rec} acts as a Huygens secondary source in Eq. (2), projecting waves to the active boundary S^{src} (Baker and Copson, 1950). The projected waves can arrive at the physical non-monopole-like sources at S^{src} in a variety of directions. If the physical sources at S^{src} all have the same radiation pattern, one can apply the filters $\hat{W}(\theta, f)$ to compensate for all of these non-monopolar radiation patterns. In the f-k domain, the direction of waves arriving at the active boundary S^{src} is known explicitly for each value of f/k as long as the local wave speed c_0 is known, so the non-monopole-like radiation pattern can be incorporated into the pre-computed Green's functions. Note that the above scheme is purely a processing method that compensates for the radiation pattern of active sources and does not involve potential reciprocal issues in the representation theorem (Aki and Richards, 2002). That is, no reciprocal exchange between sources and receivers in Green's functions such as $G(\mathbf{x}_{src}, t, \mathbf{x}_{rec}, 0)$ and $\Gamma(\mathbf{x}_{src}, t, \mathbf{x}_{rec}, 0)$ in Eq. (2) is carried out, and the processing in Eqs. (8) and (9) for each receiver (or equivalently each Huygens secondary source) at the recording surface S^{rec} relies on the assumption that physical sources on S^{src} are well manufactured to have a common (non-monopolar) radiation pattern. However, the immersive or exact boundary condition theory that is the heart of Eqs. (1) and (2) involves source-receiver reciprocity with a homogenous boundary condition (a rigid boundary condition) assumed (van Manen *et al.*, 2007).

III. NUMERICAL EXAMPLES

A. Model and reference simulation

The numerical modeling in this paper is performed similarly to that in Broggini *et al.* (2017) using a two-dimensional staggered finite-difference framework with second-order accuracy in space and time. In 2D simulations, a point source effectively represents a line source with the length presumably infinite in the third dimension. The Green's functions such as those in Eq. (2) are numerically computed with a time-domain impulsive source in finite-difference simulations (see also Mittet, 1994). For the finite-difference modeling of a physical source with a non-monopole-like radiation pattern, we inject a source signature $q(t)$ at nine adjacent points on the pressure grid as shown in Fig. 5. For each grid point with number i ($i = 1, 2, \dots, 9$), the injected source signature is scaled by a factor P_i such that $P_i \times q(t)$ is the injected source function at point i . The coefficients P_i can be chosen in numerical simulations to create a

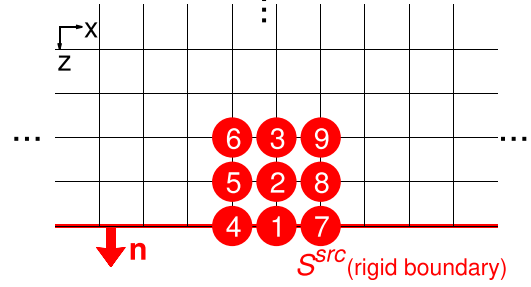


FIG. 5. (Color online) Schematic illustration of nine-point injection on the pressure grid for a non-monopole-like source. The nine points are numbered from 1 to 9. The black lines denote the pressure grid in finite-difference modeling while the red line denotes the rigid boundary on which active sources are mounted in immersive wave control experiments.

source with a certain radiation pattern. Table I lists the coefficients P_i for two kinds of non-monopolar radiation patterns I and II. With the receiver geometry given in Fig. 2, one can measure the radiation pattern with a radius $R = 35 \times dx$. Figure 6 shows the measured radiation patterns with a Ricker wavelet $q(t)$ as the source signature. The Ricker wavelet is the second derivative of a Gaussian [see Wang (2015), and references therein] and is broadband in its frequency spectrum where the highest frequency f_{max} is 2.5 times of the peak frequency f_p (i.e., the most energetic frequency) while the lowest frequency is approximately 10 times smaller than f_p . Radiation pattern I has a weak directional dependence approximately corresponding to 3 dB variation in strength, meaning 23% variation in loudness (amplitude) or half-power difference between the wave energy received at the normal direction $-n$ and its perpendicular. In the laboratory, the 3 dB source directivity threshold is often used to quantitatively define a physical source as effectively monopolar (Kinsler *et al.*, 2000). Radiation pattern II has a strong directional dependence and means sources with a significant strength of radiation variation. The nine-point scheme is a simple and computationally efficient way to simulate physical sources with some radiation patterns (see also Landrø, 1993) compared to computationally more expensive finite-element simulations that incorporate piezoelectrical physics (e.g., Simkovics *et al.*, 1999; Willard, 2019; Willard *et al.*, 2018).

Figure 7 shows a 2D test model with homogeneous velocity c_0 and density heterogeneities in both virtual and simulated physical domains. The reference simulation (upper snapshot in each panel of Fig. 8) is performed in the model shown in Fig. 7 without the rigid boundary to show the ideal wavefield when the physical domain is perfectly linked to the virtual domain. For this simulation, perfectly matched layers (PMLs) (e.g., Roden and Gedney, 2000) are implemented to absorb the out-radiating wavefield outside of the

TABLE I. Coefficients P_i for the nine-point injection scheme used to simulate physical sources. RP denotes “radiation pattern.”

	P_1	P_2	P_3	P_4	P_5	P_6	P_7	P_8	P_9
RP I	0.33	0.12	-0.08	0.14	0.21	-0.24	0.23	0.26	-0.23
RP II	0.51	-0.22	-0.50	0.25	0.40	-0.44	0.67	0.48	-0.21

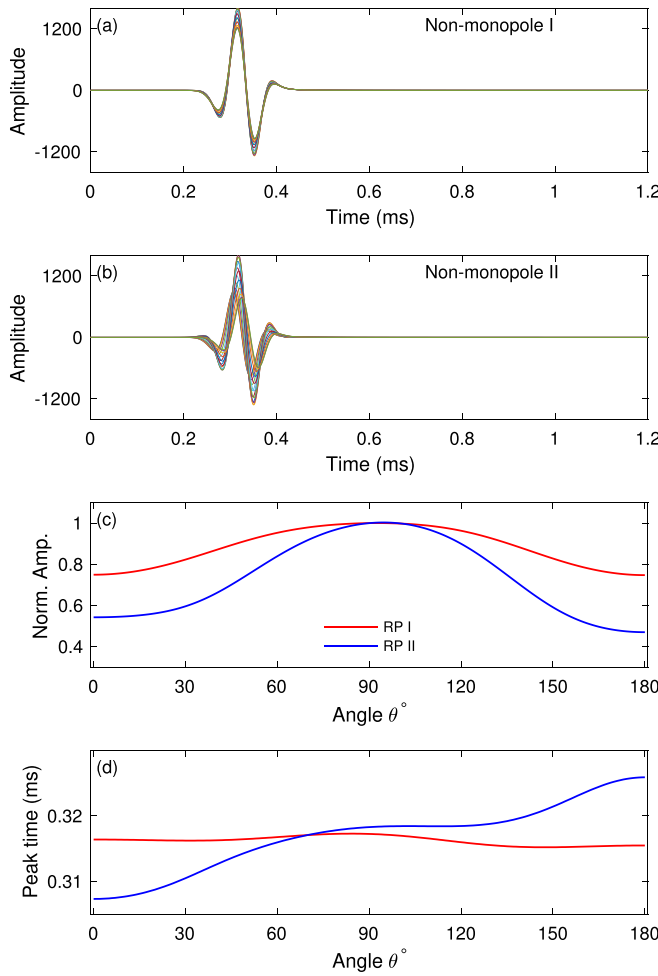


FIG. 6. (Color online) Measured radiation patterns of the two nine-point sources with coefficients P_i given in Table I. Graphs (a) and (b) show the signals received over a range of directions $\theta = 0^\circ - 180^\circ$ for non-monopole-like sources I and II. Graph (c) shows the amplitude variation of these signals with θ while graph (d) shows the time of the peak-amplitude arrivals.

model region. Table II summarizes the model and simulation parameters used. The grid size can be expressed as $dx = 0.125 \times c_0/f_{\max}$, which means 8 grid point samples per shortest wavelength in numerical simulations. The high aspect ratio of the model (Fig. 7) ensures that primary outgoing waves [e.g., ray path 1 in Fig. 1(a)] arrive at the active source boundary S^{src} with a broad range of incident angles,

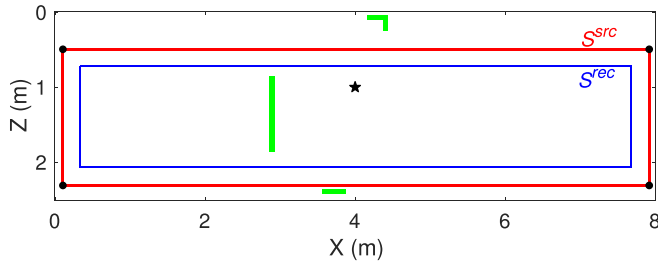


FIG. 7. (Color online) Two-dimensional density model with background density ρ_0 (white region), and with linear and corner scatterers of density $6\rho_0$ (green) in both virtual and simulated physical domains. The recording surface S^{rec} is shown as a blue rectangle while the active source boundary S^{src} is shown in red. The active boundary S^{src} contains densely distributed nine-point sources, and a one-point source (i.e., a monopole) at each of the four corners (black dots). The black star denotes a pressure source that generates wave energy for the acoustic experiment.

which helps to assess both the influence (Sec. III B) and compensation (Sec. III C) of non-monopole-like radiation patterns in active wave control experiments.

Figure 8 shows a numerically simulated immersive wave control experiment with monopolar sources on the active boundary S^{src} (middle snapshots in each panel). The corresponding movie is Mm. 1. Here the interior “physical” domain has been numerically simulated, which gives us access to the full wavefield at every point in the medium. In a real physical experiment, real waves would propagate in the interior domain containing physical scatterers, but otherwise the simulated results are similar to those from a real experiment if truly monopolar sources were available. The difference panels in Fig. 8 demonstrate that the numerical immersion of a simulated physical domain into a virtual domain using monopolar sources is accurate to machine-precision with the error at a relative order of magnitude of 10^{-12} (see also Broggini *et al.*, 2017). Out-going waves are canceled as they arrive at the rigid boundary and in-going waves are produced in the simulated physical domain, giving the acoustic illusion within the physical domain that all waves propagate as if the physical domain is seamlessly connected to a surrounding virtual domain.

Mm. 1. Simulated immersive wave control experiment with monopolar sources. This is a file of type “mov” (1.8 Mb).

B. Influence of source radiation patterns

Figure 9 shows a simulated immersive wave control experiment conducted with non-monopole-like sources of type I parametrized by the nine-point scheme shown in Fig. 5 and the coefficients P_i in Table I (“RP I”). The corresponding movie is Mm. 2. In this case the immersive wave control experiment uses the standard Eqs. (2) and (3), and hence does not compensate for source radiation patterns. The influence of the non-monopole-like radiation pattern I is indicated in Fig. 9 mainly as uncanceled out-going wave energy (denoted “out-going effect”). Note that the coefficients P_i for the non-monopole-like radiation pattern are normalized so as to produce the equivalent intensity to a monopolar source in the normal direction; hence, the influence of the non-monopolar radiation pattern is not simply caused by a scaling factor that controls the strength of the sources in the simulated immersive experiment. Figure 10 shows the recorded signals at the location of the black triangle in Fig. 9. Four main arrivals are visible in the “reference” trace again showing that the cancellation of primary out-going waves at the active boundary S^{src} is erroneous. Arrivals 2 and 4 represent the first-order interaction between the simulated physical domain and virtual domain, and the immersive wave control experiment also contains higher-order scattering between the two domains that is recorded at the receiver (black triangle) with low amplitude, as denoted by “higher-order” in the middle panel of Figs. 9(d) and 10(a). However, Figs. 9 and 10(a) do not clearly reveal the influence of the radiation pattern on producing the in-going waves backscattered from the virtual domain.

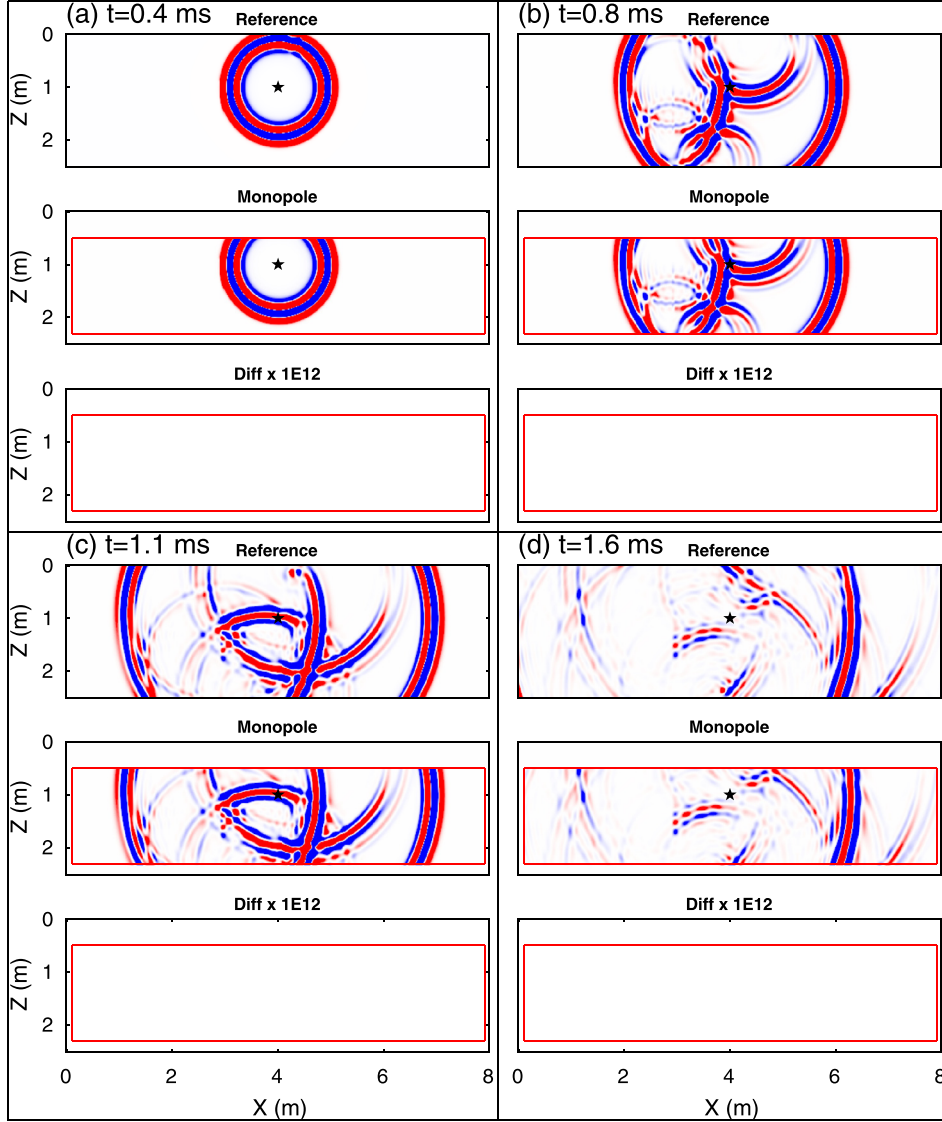


FIG. 8. (Color online) Simulated immersive wave control experiment with monopolar sources on the active boundary S^{src} (red box). Each panel shows a snapshot of the reference simulation (upper), the propagating wavefield in the immersive experiment (middle), and the difference between the two simulations in the simulated physical domain at time t (lower). The black star denotes the local source in the experiment. The corresponding movie is [Mm. 1](#).

[Mm. 2](#). Simulated immersive wave control experiment with non-monopolar sources I. This is a file of type “mov” (2.6 Mb).

Figure 11 shows a simulated immersive wave control experiment with non-monopole-like sources II (“RP II” in Table I), and Fig. 12 shows the recorded signals at the location of the black triangle in Fig. 11. The corresponding

TABLE II. Numerical values of the model parameters used.

Parameter	Definition	Value
c_0	acoustic velocity	3000 m/s
ρ_0	background density	2000 kg/m ³
l_x	length of model	8 m
l_z	width of model	2.5 m
f_p	peak frequency of Ricker wavelet	10 kHz
f_{max}	maximum frequency of Ricker wavelet	25 kHz
t_{max}	time length of simulation	2.2 ms
dt	time step	1.5×10^{-6} s
dx	finite-difference grid size in x direction	$0.015 \text{ m} (\frac{1}{8} c_0 / f_{max})$
dz	finite-difference grid size in z direction	$0.015 \text{ m} (\frac{1}{8} c_0 / f_{max})$

movie is [Mm. 3](#). In addition to the influence of the radiation pattern on the out-going waves, the influence on the production of in-going waves at the active boundary is also observed as denoted by “in-going effect” for arrival 2 in Figs. 11(b) and 12. The produced in-going waves such as arrival 2 have incorrect amplitudes compared to those in the reference simulation. In addition, the influence of radiation pattern II in Figs. 11 and 12 is more prominent with stronger undesired scattering than that of radiation pattern I in Figs. 9 and 10(a), since waves from sources II have a stronger directional dependence than those from non-monopolar sources I, as shown in Fig. 6. We also note that the influence of the radiation patterns in Figs. 9 and 11 are kinematically alike, and Figs. 10(a) and 12 show that the kinematics (ray geometry) of the out-going reflection in recorded (red) traces for sources I and II are (almost) identical. These examples imply that errors due to non-monopolar radiation patterns are mainly a dynamic effect.

[Mm. 3](#). Simulated immersive wave control experiment with non-monopolar sources II. This is a file of type “mov” (3.5 Mb).

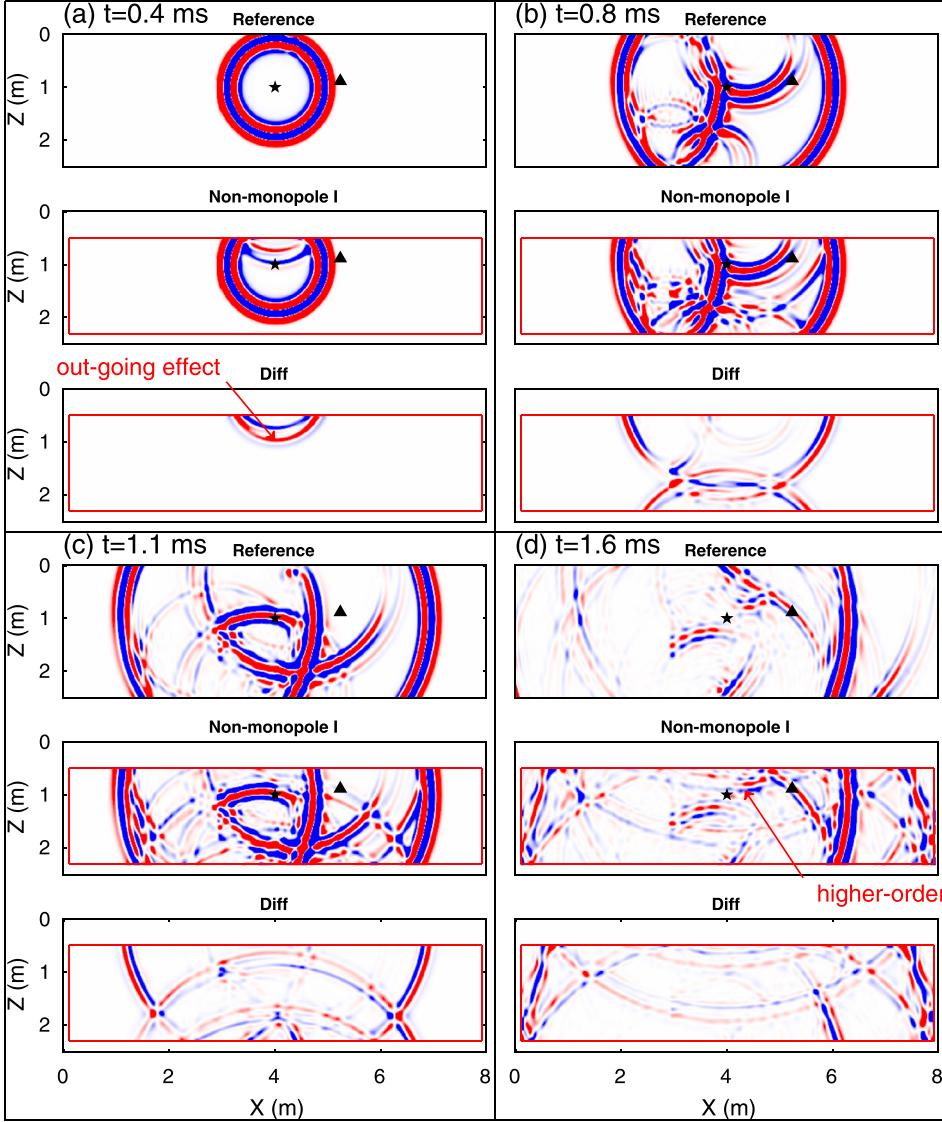


FIG. 9. (Color online) Simulated immersive wave control experiment with non-monopolar sources I. The black triangle denotes a receiver in both the immersive wave control experiment (middle panel) and reference simulation (upper panel). Otherwise, key as in Fig. 8. The corresponding movie is [Mm. 2](#).

Sources with a non-monopole-like radiation pattern have a very significantly first-order impact on the performance of active boundaries such as S^{src} , even when source performance lies within the 3 dB tolerance in vertical angle variation usually applied to define monopole-like behavior. The non-monopole-like active sources fail to fully cancel out-going waves in the immersive experiments so that the rigid boundary causes reflections in the simulated physical domain. As a result, reflected wave energy remains in the interior domain for the entire experiment, and Figs. 10(a) and 12 show the strength of the undesired reflected waves such as the distinct “out-going reflection” between the main arrivals 1 and 2. The production of in-going waves is kinematically correct but dynamically incorrect [denoted “in-going effect” in Figs. 11(b) and 12].

C. Compensation of non-monopolar radiation patterns

Figure 13 shows the simulated immersive wave control experiment with the non-monopole-like sources I [Eq. (10)] and the compensation method in Sec. II applied [Eq. (11)]. The corresponding movie is [Mm. 4](#). The directive matched filters used in Eqs. (8) and (9) are computed by deconvolving

the signals received in each direction θ separately in the configuration of Fig. 2 for a monopolar and non-monopolar source with a Ricker wavelet as the source signature. These signals from the two types of non-monopolar sources are shown in Figs. 6(a) and 6(b), and the deconvolution is carried out in the frequency domain by a division per frequency with a water level or regularization factor, which is searched in an ad-hoc way ([Press et al., 2007](#)). The resultant directive matched filters will stay in the frequency domain and be further used in the frequency-wavenumber domain as in Eqs. (8) and (9). For such a radiation pattern with weak directivity (<3 dB), the influence of the non-monopole-like radiation pattern in immersive experimentation has been fully corrected with a negligible residual error. The out-going reflection observed in Fig. 9(a) is successfully suppressed, and the waveform of the recorded signal for the four arrivals is correct compared to the reference trace, as shown in Fig. 13(e).

Mm. 4. Simulated immersive wave control experiment with the non-monopolar sources I and f-k processing method applied (“Comp RP”). This is a file of type “mov” (1.9 Mb).

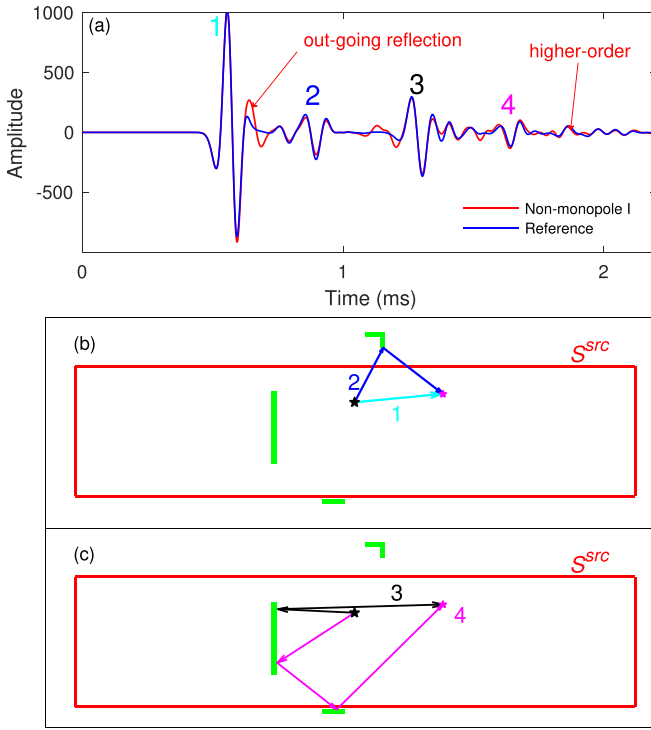


FIG. 10. (Color online) (a) Recorded traces at the location of the black triangle in Fig. 9 for the reference and immersive experiment with non-monopolar sources I. Four arrivals in the reference trace are denoted and correspond to the schematic ray paths in graphs (b) and (c).

Figure 14 shows the simulated immersive wave control experiment with the non-monopolar-like sources II and the compensation method in Sec. II applied. The corresponding movie is **Mm. 5**. Except for the non-negligible error noted in the lower panels, the influence of the non-monopolar-like radiation pattern in the immersive experiment is mostly corrected. For the out-going waves, the undesired reflection caused by the non-monopolar radiation pattern of active sources is almost suppressed since the sources project waves with the correct source amplitude and phase after directive matched filters have been applied. Some uncanceled wave energy does exist between the arrivals 1 and 2 in Fig. 14(e) for the out-going waves. However, the in-going waves such as arrival 2 in Fig. 14(e) are dynamically correct compared to the reference simulation.

Mm. 5. Simulated immersive wave control experiment with the non-monopolar sources II and f-k processing method applied (“Comp RP II”). This is a file of type “mov” (2.2 Mb).

Some errors do still exist in the result after the compensation method has been applied, caused by (1) the fact that the source distribution on the active boundary S^{src} is not continuous at the four corners at which we use monopoles since nine-point sources cannot be deployed at the corner point in finite-difference modeling, and (2) the fact that acoustic radiation patterns observed in the far-field ($R = 35 \times dx$) using the setup in Fig. 2 cannot fully account for the near-field wave sink and production process at the active boundary S^{src} . Point (1) is illustrated in Fig. 14(d) which shows a

prominent corner-point error in the lower panel, caused by the inaccurate finite-difference representation of the sources at the corner points. To further illustrate point (2), Fig. 15 shows a simple geometry that tests the application of the directive matched filter for non-monopolar source II at an angle $\theta = 60^\circ$. Either monopolar or non-monopolar sources can be placed at the black star in Fig. 15. The source signature for the monopolar source at the black star is a Ricker wavelet with the same peak frequency f_p given in Table II while the source signature for the nine-point non-monopolar source II is the Ricker wavelet convolved with the corresponding directive matched filter at an angle $\theta = 60^\circ$. In an ideal case, the radiation pattern of the non-monopolar source II should be compensated in the direction $\theta = 60^\circ$ after convolving the corresponding directive matched filter with the Ricker wavelet for the source signature. However, Fig. 16 illustrates the small near-field error close to the nine-point non-monopolar source II after compensation of the radiation pattern in one direction, compared to the near-field recordings for a monopole. Note that the source radiation pattern observed in the far field ($D = 35 \times dx$) can be well compensated in that direction ($\theta = 60^\circ$) and this is also true at all greater distances. The distance between the first receiver and source $D = 5 \times dx$ is large enough to ensure that the receiver lies outside of the nine-point region of the non-monopolar source II in the finite difference simulation. Comparing Figs. 13 and 14, one can observe that stronger source directivity results in more significant compensation errors, indicating that a simulated source with stronger directional dependence may have a larger near-field component that cannot be compensated using the method proposed in Sec. II. Although both the corner-point and compensation errors are really only features of the finite-difference simulations, these errors do have implications for laboratory immersive wave control experiments, which will be discussed in Sec. IV.

IV. DISCUSSION

A. Variable source radiation patterns

For the active boundary in each immersive experiment simulated in Sec. III, the source radiation pattern is assumed to be uniform for all active sources. While this should often be approximately true if identical sources with good quality control are used around the active boundary S^{src} , small variations in their manufacture and installation on the active boundary S^{src} does lead to variations in radiation among sources in practice (Delannoy *et al.*, 1979). We therefore now consider a set of physical sources with variable radiation patterns in immersive wave control experimentation and hence different directive matched filters $W(\mathbf{x}_{src}, \theta, t)$ for different sources mounted at \mathbf{x}_{src} . In this case, radiation patterns of all sources need to be measured off-line in the laboratory before the real-time wave control experiment. The f-k processing method proposed in Sec. II can still be used to compensate for these directivities, for example, using an accept-reject f-k processing algorithm.

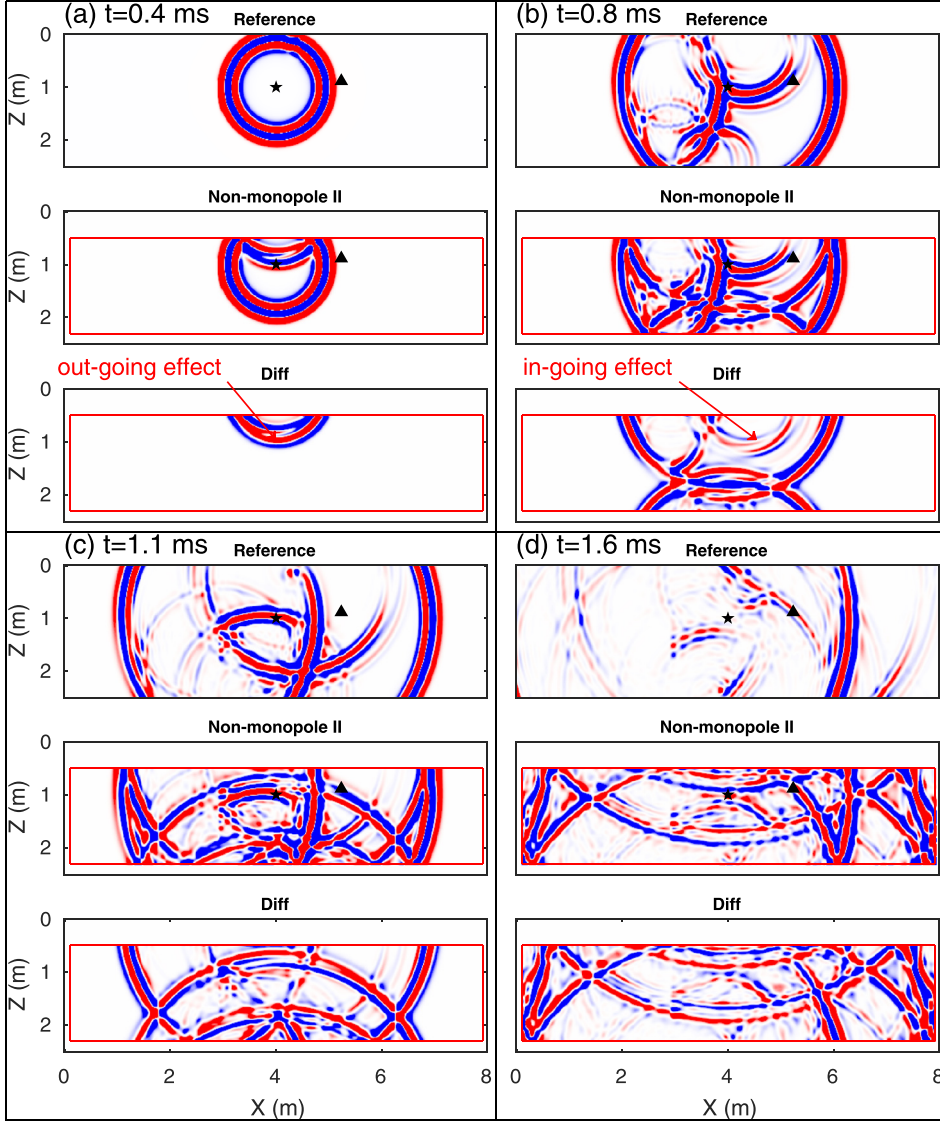


FIG. 11. (Color online) Simulated immersive wave control experiment with non-monopolar sources II. Key as in Fig. 8. The corresponding movie is Mm. 3.

- (1) Compute f-k transform of the pre-computed Green's functions using Eqs. (5) and (6) for the i th receiver location $\mathbf{x}_{i,rec}$.
- (2) For the j th physical source located at $\mathbf{x}_{j,src}$, convolve the pre-computed Green's functions with the source's directive matched filters $W(\mathbf{x}_{j,src}, \theta, t)$ using Eqs. (8) and (9). This is equivalent to replicating that particular

source's directivity for all other sources along the active boundary S^{src} .

- (3) Inverse f-k transform the processed Green's functions into the time domain and accept only the Green's function with the secondary source at $\mathbf{x}_{i,rec}$ and recording at $\mathbf{x}_{j,src}$. All other traces in the processed Green's functions are rejected since these traces do not correspond to the physical source located at $\mathbf{x}_{j,src}$ with the desired radiation pattern. Note that the Green's functions are computed numerically in the model that includes the virtual domain, where the secondary monopolar and dipolar sources are at the location of the recording surface S^{rec} in Fig. 1(b), and the recordings are at the active boundary S^{src} without a co-located rigid boundary. The physical structure of the medium inside S^{rec} is irrelevant and can be set arbitrarily when computing these Green's functions.
- (4) Repeat steps (2) and (3) for all sources with respect to the receiver at $\mathbf{x}_{i,rec}$, thus producing the processed Green's functions $\tilde{G}(\mathbf{x}_{src}, t, \mathbf{x}_{i,rec}, 0)$ and $\tilde{\Gamma}(\mathbf{x}_{src}, t, \mathbf{x}_{i,rec}, 0)$.
- (5) Repeat steps (1), (2), (3), and (4) for all receivers on the recording surface S^{rec} and so obtain the processed

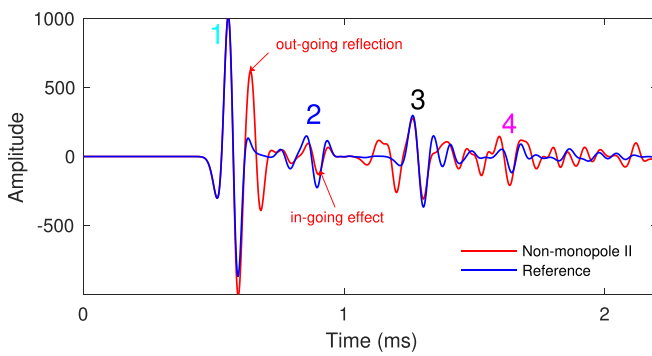


FIG. 12. (Color online) Recorded traces at the location of the black triangle in Fig. 11 for the reference and immersive experiment with non-monopolar sources II.

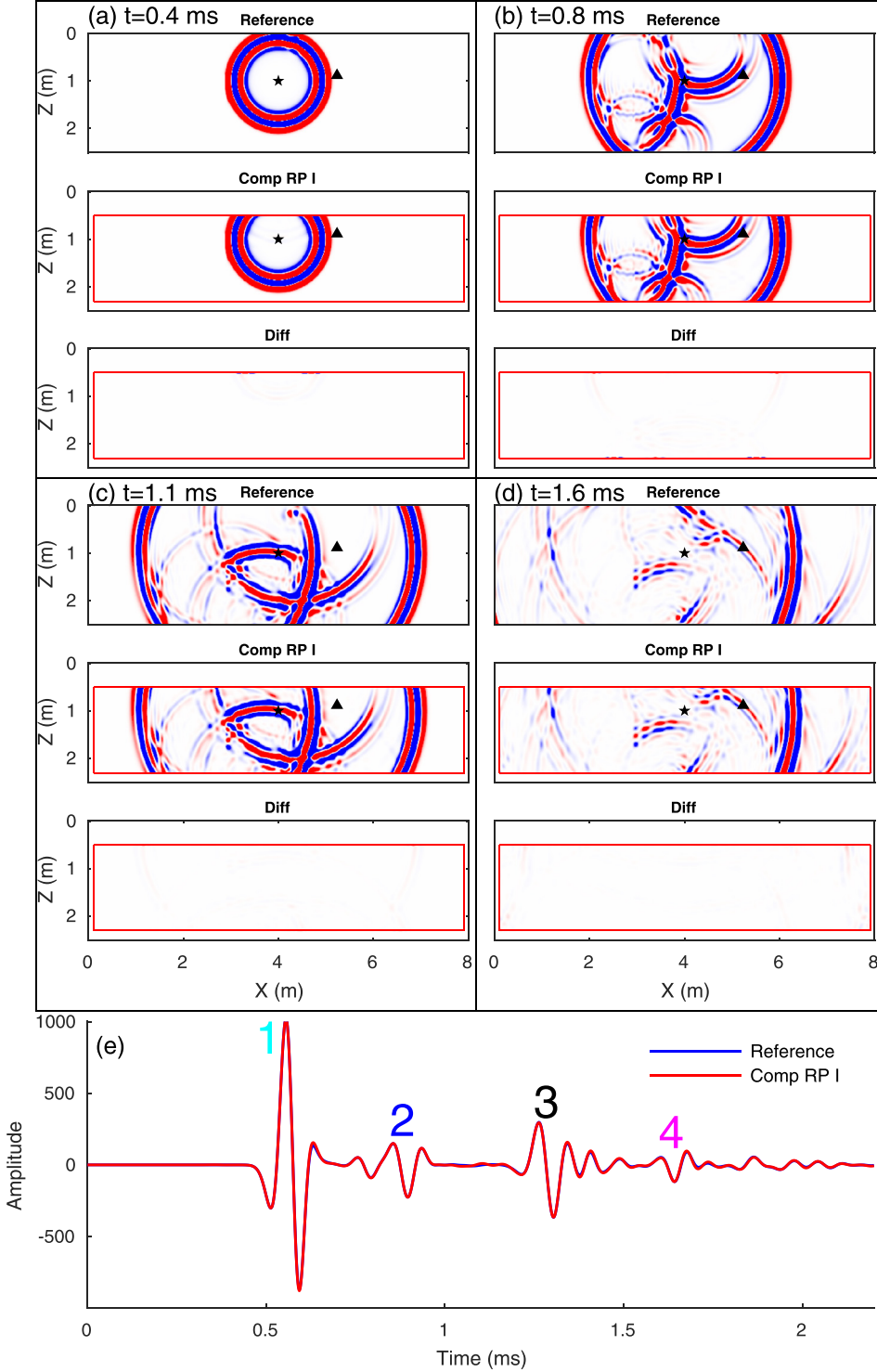


FIG. 13. (Color online) Simulated immersive wave control experiment with the non-monopolar sources I and f-k processing method applied (“Comp RP I”). (e) Recorded traces at the location of the black triangle. The four arrivals correspond to the schematic ray paths in Figs. 10(b) and 10(c). Key for (a) to (d) as in Fig. 8. The corresponding movie is Mm. 4.

monopole and dipole Green’s functions $\tilde{G}(\mathbf{x}_{src}, t, \mathbf{x}_{rec}, 0)$ and $\tilde{\Gamma}(\mathbf{x}_{src}, t, \mathbf{x}_{rec}, 0)$, which can be applied in immersive wave control experiments using Eqs. (10) and (11).

The above accept-reject processing method is demonstrated in the following numerical example. We first create a set of nine-point sources with different non-monopole-like radiation patterns whose nine-point coefficients are numerically generated by varying the coefficients of radiation pattern II in Table I by a random amount within the range $[-0.05, 0.05]$. Figure 17 shows the radiation patterns of these

sources as measured using the geometry ($R = 35 \times dx$) given in Fig. 2. The model in Fig. 7 and parameters in Table II are used, and Fig. 18 shows the simulated immersive wave control experiment with the set of non-monopolar sources and the above accept-reject processing method applied. The corresponding movie is Mm. 6. Compared to Fig. 14 with non-monopolar source II, the compensation error in Fig. 18 is quite strong since many nine-point sources have stronger radiation patterns than that of non-monopolar source II, and hence result in higher modeling (near-field) errors. In particular, some source radiations have unconventional patterns

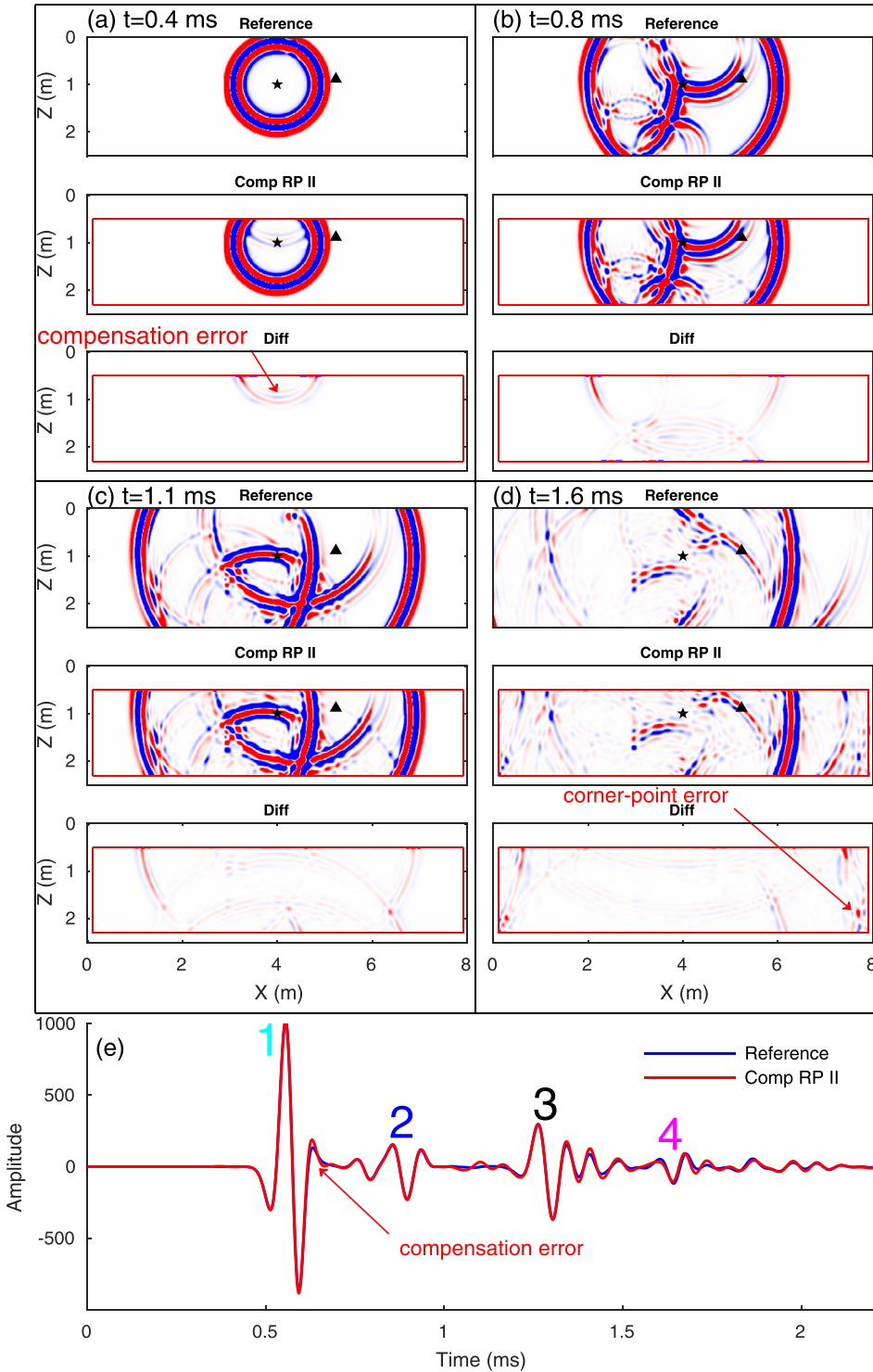


FIG. 14. (Color online) Simulated immersive wave control experiment with the non-monopolar sources II and f-k processing method applied (“Comp RP II”). (e) Recorded traces at the location of the black triangle. Key for (a) to (d) as in Fig. 8. The corresponding movie is Mm. 5.

compared to non-monopolar source II, and Fig. 17 indicates one unconventional radiation pattern as an example. Such an unconventional radiation pattern is physically possible when the piezoelectric structure of a transducer is not well manufactured and involves flexural modes which result in unexpected resonances (Willard, 2019; Willard *et al.*, 2018; Woollett and Finch, 1990). However, the compensation error is still not comparable to the propagating wavefield in the simulated physical domain [see Fig. 18(e)], and the waveform of the recorded signal at the location of the black triangle in the immersive wave control experiment is

approximately correct compared to the reference simulation. We conclude that physical sources with variable radiation patterns do not significantly influence the performance of the compensation method.

Mm. 6. Simulated immersive wave experiment with the non-monopolar sources with variable radiation patterns and f-k processing method applied (“Comp RP V”). This is a file of type “mov” (2.4 Mb).

The above numerical examples and those in Sec. III demonstrate that the compensation method in Sec. II enables

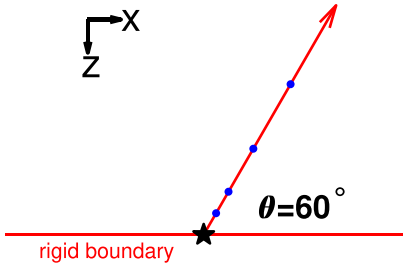


FIG. 15. (Color online) Geometry used to test the application of the directive matched filters [Eq. (4)] at an angle $\theta = 60^\circ$ for receivers (blue dots) with distances ($D = 5, 10, 20, 35 \times dx$) to the source (black star).

non-monopole-like active sources to be used to cancel outgoing waves and produce in-going waves in immersive wave control experiments, as illustrated in Fig. 4. The method does not require any wavefield separation into in- and outgoing components (Robertsson and Curtis, 2002; Thomson, 2012), and in-going waves entering the physical domain which then become out-going waves are correctly canceled when they arrive at the rigid boundary. Hence, the so-called long-term, higher-order interaction [e.g., energy denoted “higher-order” in Fig. 9, see also Broggini *et al.* (2017)] between the simulated physical and virtual domains is also implemented correctly using non-monopole-like sources.

Source radiation patterns have to be measured when the source is installed onto the rigid boundary of the experimental setup since the rigid boundary and installation

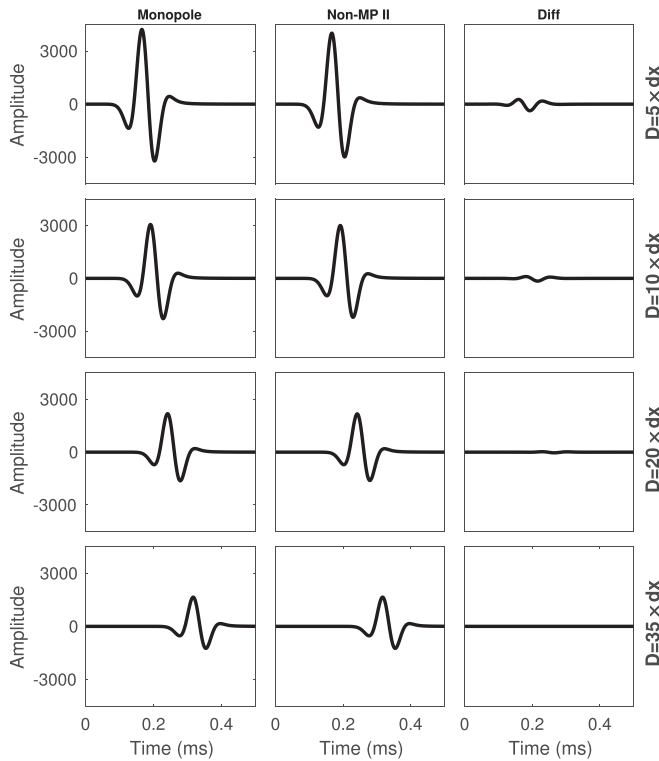


FIG. 16. Recorded signals at the receivers in Fig. 15. The first column (“monopole”) gives the recorded signals for the monopole at a distance $D = 5, 10, 20, 35 \times dx$ while the second column (“Non-MP II”) gives the signals for non-monopolar source II with the application of the directive matched filter in the direction of the receiver array shown in Fig. 15. The third column (“Diff”) shows the difference between the signals in the first and second columns.

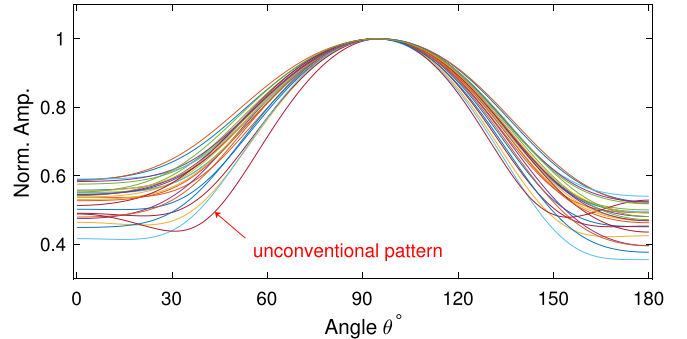


FIG. 17. (Color online) Measured radiation patterns of a set of simulated sources with random 9-point coefficients. Key as Fig. 6(c).

influence the radiation pattern of active sources (Delannoy *et al.*, 1979). The source directivity is also influenced by the frequencies of the emitted waves. Note that in the laboratory, the impulsive recordings \tilde{M}^p in Eq. (4) may not be possible, and one can replace \tilde{M}^p by responses of a physical source with a wavelet signature and keep that wavelet signature when producing the monopolar responses that replace M^p . The wavelet signature used for computation of the directive matched filters should cover the whole wave bandwidth of the immersive wave control experiment. When the measurement of the source radiation pattern involves a source wavelet that has the same frequency bandwidth as that in the immersive wave control experiments, the compensation of source directivity occurs for every frequency in the immersive experiments. The measurement geometry in Fig. 2 could be spatially limited when the source is close to the corner of the experimental setup, such as in a water tank for example.

B. Insights into the compensation of source radiation patterns

One can regard the f-k processing method proposed in Sec. II as equivalent to spatio-temporal calibration of physical sources in all 2D (or 3D) directions. The directive matched filters in Eq. (4) calibrate the amplitude and phase of the emitted wavefield from $\hat{P}^{IBC}(\mathbf{x}', t)$ in Eq. (3) to $P_{comp}^{IBC}(\mathbf{x}', t)$ in Eq. (11), accounting for the source propagation direction at the active rigid boundary. One cannot know the direction of waves arriving at the active boundary before performing the physical acoustic experiments. However, in immersive experiments with a recording surface S^{rec} , one can incorporate knowledge of the non-monopole-like radiation patterns (i.e., directive matched filters) into the pre-computed Green’s functions since source radiation patterns can be measured off-line in a homogeneous medium (Fig. 2). In addition, the immersive boundary condition [Eq. (1)] is not dependent on the details of physical wave propagation in the domain enclosed by the recording surface S^{rec} (Broggini *et al.*, 2017; Thomson, 2012).

The recording surface S^{rec} can be regarded as a (transparent) Huygens wavefront that captures the information of the out-going scattered wavefields (Baker and Copson, 1950), and hence the compensation method will not degrade due to scatterers that are located in the interior domain enclosed by S^{rec} ,

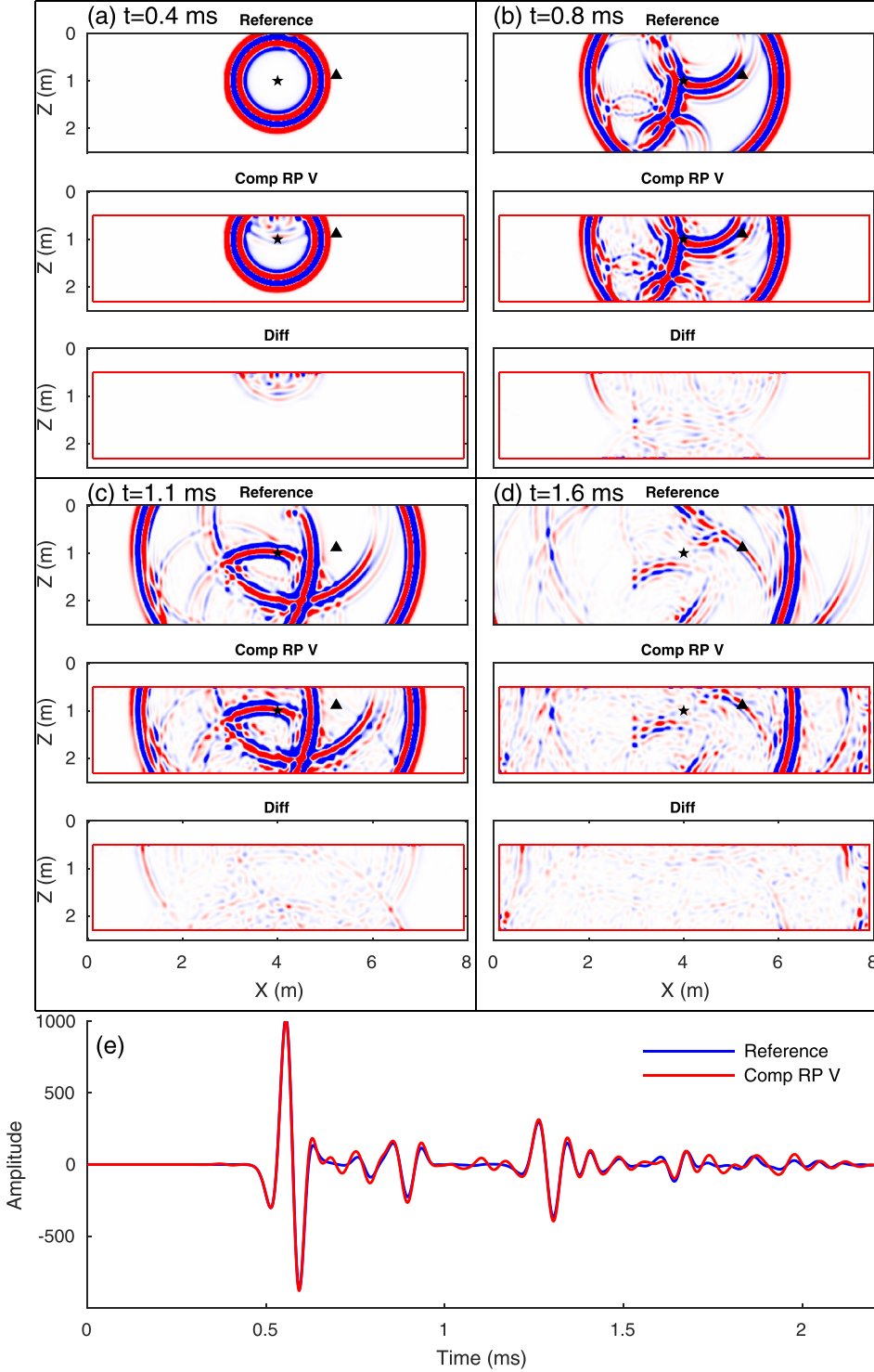


FIG. 18. (Color online) Simulated immersive wave experiment with the non-monopolar sources with variable radiation patterns and f-k processing method applied (“Comp RP V”). Key for (a) to (d) as in Fig. 8. The corresponding movie is [Mm. 6](#).

as shown in the numerical examples in Sec. III. The recording surface S^{rec} obtains the information of wave scattering between the physical and virtual domains, and active boundary S^{src} acquires that information through the Kirchhoff-Helmholtz extrapolation [Eq. (2)] in real time and embodies it within source signatures (v_n). The method in Sec. IV is demonstrated in a 2D numerical immersive wave control experiment, but generalization to a 3D framework is straightforward as the basic idea of calibrating sources according to the direction of wave reflection or propagation holds identically in a 3D f-k_x-k_y-processing scheme.

The f-k processing method in Sec. II does not give perfect compensation of the source radiation patterns in simulated immersive wave control experiments, as shown in Figs. 14 and 18. The compensation error is illustrated in Fig. 16 for the near-field imperfection regarding the application of the directive matched filters, while the corner-point error is attributed to the fact that the active boundary S^{src} mounted with non-monopolar sources is not continuous at the corners. Another way to understand the compensation error is that the active boundary S^{src} composed of nine-point non-monopolar sources cannot be considered as a perfect Huygens

surface as in Eq. (2), for which sources should involve single points of energy injection and distributed continuously around the surface (Ise, 1999). The nine-point source, shown in Fig. 5, has a part (points 5, 2, 8, 6, 3, and 9) that are displaced away from the active boundary S^{src} , hence the center of the source cannot be considered to lie exactly on S^{src} . Thus, Eq. (2) is implemented imperfectly in our scheme, so that out-going waves are not perfectly canceled. We tried using a smaller radius $R = 5 \times dx$ in Fig. 2 to calculate the directive matched filters in Eq. (4); however, in the finite-difference modeling, compensation of the source directivity in any direction was poor (not shown here). As for the corner-point error, implementing monopole injection at the corners of active boundary S^{src} is an expedient modeling compromise. The influence of the above modeling errors will decrease in the simulated immersive wave control experiments if the finite-difference grid size dx and dz is reduced. However, a decrease in the grid size reduces the directivity strength of the non-monopolar sources with the fixed coefficients P_i so that one cannot fully test the influence of a non-monopolar source with a strong radiation pattern in immersive wave control experiments without using a larger source grid than the current nine-point scheme.

Although the compensation and corner-point errors are currently only observed in the numerical synthesis of immersive wave control experiments, their observation does alert us to potential challenges in the physical implementation of the active boundary in a laboratory. From both mathematical immersive boundary condition theory (Broggini *et al.*, 2017) and 1-D physical implementations (Becker *et al.*, 2018), we understand that wavefield cancellation as well as production occurs locally at the active boundary. In immersive wave control experiments with only active sources on the rigid boundary, uncanceled and erroneous waves in the physical domain cannot be further diminished or canceled once the waves leave the boundary. Source injection therefore performs locally and exactly on the active boundary. The immersive boundary condition theory does not allow for these uncanceled waves though canceling the waves is physically possible when they arrive at the active boundary for a second time. By contrast, in the laboratory, source directivity is measured in the far field [e.g., $R = 35 \times dx$ in Fig. 2, see also IEEE (1969)], so the application of the directive matched filters in Sec. II is limited by the fact that the source radiation pattern cannot be fully compensated in the near-field (Fig. 16). This limitation depends in turn on the quality of manufacturing physical sources (e.g., the correct installation of the piezoelectric stacks) and whether each source is (fully) embedded into the active rigid boundary during installation. If physical sources are well manufactured, the undesired near-field effect of the sources should be weak and should not significantly influence the immersive wave control experiments. Also, if the near-field behavior of the active source boundary can be measured and accounted for in the laboratory (e.g., Sapozhnikov *et al.*, 2004), this limitation could be overcome using the inverse system proposed in Ise (1999) in which an optimal source injection can be inferred from the perspective of producing active boundary elements. In this case, one can iteratively adjust v_n in Eq. (10) to make $P_{comp}^{IBC}(\mathbf{x}', t)$ close to $P^{IBC}(\mathbf{x}', t)$ in Eq. (1).

A detailed parametrization of the inverse system depends on the laboratory setup of the sources on the active boundary, and can be considered in future research.

Concerns about the source radiation pattern for the design of active boundaries are particularly important for acoustic experiments in the frequency band 1–20 kHz. Below this frequency band, physical sources tend to have more isotropic radiation patterns. At frequencies higher than 20 kHz, the spatial Nyquist requirement of the active boundary becomes a dominant challenge since either one tends not to have an adequate number of transducers in the laboratory, or sources are too large to be installed on the active boundary without cross-talking or overlapping. The frequency band 1–20 kHz is of particular physical interest since the band is higher than most acoustic wave control experiments (e.g., Orduña Bustamante and Nelson, 1992; Smith *et al.*, 1999) but is lower than standard high-frequency (MHz) laboratory simulation (e.g., Blum *et al.*, 2011). Figures 9 and 10(a) demonstrate that in this frequency band even weak source directivity (<3 dB) leads to non-negligible errors in immersive wave control experiments, especially for cancellation of out-going waves. The compensation method in Sec. II addresses such concerns in the laboratory.

The compensation method for the source radiation pattern is not restricted to immersive wave control experimentation. For audio systems (e.g., Cheer, 2016; Orduña Bustamante and Nelson, 1992) with experimental frequencies smaller than 1 kHz and with directive active sources, the compensation method holds the same. Also, the compensation method does not rely on the type of active sources and should be generally applicable to various kinds of sources (e.g., piezoceramics or moving coil loudspeaker) (Moffett *et al.*, 2007; Möser and Zimmermann, 2004). The physical idea of compensating for the radiation patterns of sources according to wave propagation directions helps us to understand all wave control experiments based on Huygens principle (Baker and Copson, 1950), especially for wavefield cancellation at active boundaries. The compensation method can be extended to other wave control and synthesis experiments involving Kirchhoff-Helmholtz integrals [e.g., Berkhout *et al.* (1993); Miller (2006)]. These experiments rely on Huygens principle and are commonly formulated using continuous layers of monopolar and dipolar sources (Nelson and Elliott, 1992; Ise, 1999). The immersive wave control system is a special case where only monopolar sources are used on a rigid surface, and dipolar sources are not involved. However, the idea behind the compensation method holds the same for dipolar sources. Most wave control experiments including audio control systems (Cai *et al.*, 2014), noise minimization (Olson, 1956) and cloaking (Cheer, 2016; Liu *et al.*, 2018) are based on inversion methods where source injection at the active boundary is determined by the received signal at one or more receivers in an interior physical domain (e.g., Guicking and Karcher, 1984; Poletti and Fazi, 2015). Compared to these wave control experiments, an immersive wave control experiment uses a recording surface S^{rec} to determine the source injection at the active boundary in real time, which can be considered as an exact forward solution for the wavefield control. In

addition, immersive experimentation takes higher-order interaction between the experimental setup and virtual domain into account; hence, the produced wavefield can be (fully) re-canceled when it next interacts with the active boundary. In contrast to such an immersive active boundary, other active boundary designs only work well for first-order interactions such as primary wave cancellation or production (Nelson, 1994; Williams, 1984): the waves produced at the active boundary cannot be fully canceled when they arrive at the boundary for a second time. On the other hand, using an immersive active boundary as a forward wave control solution based on a representation theorem and a Kirchhoff-Helmholtz integral requires more stringent tolerances on equipment such as source directivity than other active boundaries where adaptive inversion schemes could account for the source directivity to some extent. Herein we show how to adjust for differences between real-world equipment used to construct immersive boundaries and the requirements of the acoustic wave theory that is assumed to hold. Since we can correct the performance of this more stringent case, other types of active boundaries can be improved using the same methodology.

V. CONCLUSION

Active source boundaries around physical experiments can create an artificial immersive environment where the physical setup is perfectly linked to a virtual domain that contains arbitrarily complex objects. Such wave control experiments face the challenge of using non-monopolar sources at the active boundary, which do not conform to theoretical boundary conditions. Anisotropic source radiation patterns cause a dynamic error in immersive wave control experiments, so that wave cancellation and production at the active boundary is imperfect.

Based on Huygens principle interpreted in the Kirchhoff-Helmholtz integral, acoustic radiation patterns of active sources used in immersive experimentation can be compensated with a pre-processing method that is applied to the pre-computed Green's functions used in the Kirchhoff-Helmholtz integral. The processing method involves (a) computing directive matched filters, (b) transforming the Green's functions into the frequency-wavenumber (f-k) domain, (c) identifying the direction of wave propagation in the Green's functions, (d) incorporating the directive matched filters into the Green's functions in the f-k domain, (e) inverse-transforming the processed Green's functions to the time domain, and (f) conducting immersive wave control experiments using the processed Green's functions. We demonstrate that the method is effective through finite-difference modeling in which the true solution or ideal wave immersion is known for comparison. Thus, we present a practical solution that can be used to compensate for source radiation patterns on active boundaries in laboratories or other environments. The method can be applied to acoustic wave synthesis experiments in 2D and 3D involving Kirchhoff-Helmholtz integrals and Huygens principle. It does not impede real-time computation in immersive experimentation as it only modifies

Green's functions that are pre-computed before conducting the experiments. Our work enables acoustically linking a physical domain to a virtual domain using active sources with non-monopole-like radiation patterns, which do not fit into the ideal immersive boundary condition theory. Hence, non-monopolar sources can now be used in the laboratory for immersive wave control experiments.

ACKNOWLEDGMENTS

We thank two anonymous reviewers for their positive and constructive comments. We would like to thank Erik Koene and Dr. Filippo Broggini for insightful discussions of the immersive boundary condition theory, and Nele Börsing for discussions about the acoustic radiation patterns of practical sources. We thank Dr. Cedric Schmelzbach and Dr. Fredrik Andersson for discussions about the directive matched filters designed in this paper. This project has received funding from the European Research Council (ERC) under the European Union's Horizon 2020 research and innovation programme (Grant Agreement No. 694407).

- Aki, K., and Richards, P. (2002). *Quantitative Seismology*, in *Geology (University Science Books): Seismology* (University Science Books, Sausalito, CA).
- Baker, B., and Copson, E. (1950). *The Mathematical Theory of Huygens' Principle* (Clarendon Press, Oxford).
- Becker, T. S., van Manen, D.-J., Donahue, C. M., Bärlocher, C., Börsing, N., Broggini, F., Haag, T., Robertsson, J. O. A., Schmidt, D. R., Greenhalgh, S. A., and Blum, T. E. (2018). "Immersive wave propagation experimentation: Physical implementation and one-dimensional acoustic results," *Phys. Rev. X* **8**(3), 031011.
- Berkhout, A. J., de Vries, D., and Vogel, P. (1993). "Acoustic control by wave field synthesis," *J. Acoust. Soc. Am.* **93**(5), 2764–2778.
- Beyene, S., and Burdisso, R. A. (1997). "A new hybrid passive-active noise absorption system," *J. Acoust. Soc. Am.* **101**(3), 1512–1515.
- Blum, T. E., van Wijk, K., Snieder, R., and Willis, M. E. (2011). "Laser excitation of a fracture source for elastic waves," *Phys. Rev. Lett.* **107**, 275501.
- Börsing, N., Becker, T. S., Curtis, A., van Manen, D.-J., Haag, T., and Robertsson, J. O. A. (2019). "Cloaking and holography experiments using immersive boundary conditions," *Phys. Rev. Appl.* **12**, 024011.
- Broggini, F., Vasmel, M., Robertsson, J. O. A., and van Manen, D.-J. (2017). "Immersive boundary conditions: Theory, implementation, and examples," *Geophysics* **82**(3), T97–T110.
- Cai, Y., Wu, M., and Yang, J. (2014). "Sound reproduction in personal audio systems using the least-squares approach with acoustic contrast control constraint," *J. Acoust. Soc. Am.* **135**(2), 734–741.
- Camras, M. (1968). "Approach to recreating a sound field," *J. Acoust. Soc. Am.* **43**(6), 1425–1431.
- Cheer, J. (2016). "Active control of scattered acoustic fields: Cancellation, reproduction and cloaking," *J. Acoust. Soc. Am.* **140**(3), 1502–1512.
- Coleman, P., Jackson, P. J. B., Olik, M., Mäzller, M., Olsen, M., and Abildgaard Pedersen, J. (2014). "Acoustic contrast, planarity and robustness of sound zone methods using a circular loudspeaker array," *J. Acoust. Soc. Am.* **135**(4), 1929–1940.
- Delannoy, B., Lasota, H., Bruneel, C., Torguet, R., and Bridoux, E. (1979). "The infinite planar baffles problem in acoustic radiation and its experimental verification," *J. Appl. Phys.* **50**(8), 5189–5195.
- Ebrom, D., and McDonald, J. (1994). *Seismic Physical Modeling*, Vol. 15 of *Cruisin'* (Capstone) (Society of Exploration Geophysicists, Tulsa, OK).
- Givoli, D., and Cohen, D. (1995). "Nonreflecting boundary conditions based on Kirchhoff-type formulae," *J. Comput. Phys.* **117**(1), 102–113.
- Guicking, D., and Karcher, K. (1984). "Active impedance control for one-dimensional sound," *J. Vib. Acoust. Stress. Reliab. Des.* **106**, 393–396.
- IEEE (1969). "IEEE standard definitions of terms for antennas," *IEEE Trans. Ant. Propag.* **17**(3), 262–269.
- Ise, S. (1999). "A principle of sound field control based on the Kirchhoff-Helmholtz integral equation and the theory of inverse systems," *Acta*

- Acust. Acust. **85**, 78–87, available at <https://www.semanticscholar.org/paper/A-principle-of-sound-field-control-based-on-the-and-Ise/90e3d8c3ce33471d4079a0bd6bbf081ed931b9#paper-header>.
- Kinsler, L., Kinsler, L., Frey, A., Coppens, A., and Sanders, J. (2000). *Fundamentals of Acoustics* (Wiley, New York).
- Kirkeby, O., and Nelson, P. A. (1993). “Reproduction of plane wave sound fields,” *J. Acoust. Soc. Am.* **94**(5), 2992–3000.
- Landrø, M. (1993). “Implementing measured source signatures in a coarse-grid, finite-difference modeling scheme,” *Geophysics* **58**(12), 1852–1860.
- Liu, J., Wang, X., Wu, M., and Yang, J. (2018). “An active control strategy for the scattered sound field control of a rigid sphere,” *J. Acoust. Soc. Am.* **144**(1), EL52–EL58.
- Miller, D. A. B. (1991). “Huygens’s wave propagation principle corrected,” *Opt. Lett.* **16**(18), 1370–1372.
- Miller, D. A. B. (2006). “On perfect cloaking,” *Opt. Express* **14**(25), 12457–12466.
- Mittet, R. (1994). “Implementation of the Kirchhoff integral for elastic waves in staggered-grid modeling schemes,” *Geophysics* **59**(12), 1894–1901.
- Moffett, M. B., Robinson, H. C., Powers, J. M., and Baird, P. D. (2007). “Single-crystal lead magnesium niobate-lead titanate (PMN/PT) as a broadband high power transduction material,” *J. Acoust. Soc. Am.* **121**(5), 2591–2599.
- Möser, M., and Zimmermann, S. (2004). *Engineering Acoustics: An Introduction to Noise Control* (Springer, Berlin).
- Nelson, P. (1994). “Active control of acoustic fields and the reproduction of sound,” *J. Sound. Vib.* **177**(4), 447–477.
- Nelson, P., and Elliott, S. (1992). *Active Control of Sound* (Academic Press, New York), Bd. 3.
- Olson, H. F. (1956). “Electronic control of noise, vibration, and reverberation,” *J. Acoust. Soc. Am.* **28**(5), 966–972.
- Orduña Bustamante, F., and Nelson, P. A. (1992). “An adaptive controller for the active absorption of sound,” *J. Acoust. Soc. Am.* **91**(5), 2740–2747.
- Poletti, M. A., and Fazi, F. M. (2015). “An approach to generating two zones of silence with application to personal sound systems,” *J. Acoust. Soc. Am.* **137**(2), 598–605.
- Press, W., Teukolsky, S., Vetterling, W., and Flannery, B. (2007). *Numerical Recipes: The Art of Scientific Computing*, 3rd ed. (Cambridge University Press, Cambridge).
- Robertsson, J. O. A., and Curtis, A. (2002). “Wavefield separation using densely deployed three-component single-sensor groups in land surface-seismic recordings,” *Geophysics* **67**(5), 1624–1633.
- Roden, J. A., and Gedney, S. D. (2000). “Convolution PML (CPML): An efficient FDTD implementation of the CFS-PML for arbitrary media,” *Microw. Opt. Technol. Lett.* **27**(5), 334–339.
- Sapozhnikov, O. A., Morozov, A. V., and Cathignol, D. (2004). “Piezoelectric transducer surface vibration characterization using acoustic holography and laser vibrometry,” in *IEEE Ultrasonics Symposium, 2004*, Vol. 1, pp. 161–164.
- Sherman, C., and Butler, J. (2007). *Transducers and Arrays for Underwater Sound*, in *The Underwater Acoustics Series* (Springer, New York).
- Simkovics, R., Landes, H., Kaltenbacher, M., and Lerch, R. (1999). “Nonlinear finite element analysis of piezoelectric transducers,” in *Proceedings of 1999 IEEE Ultrasonics Symposium*, Vol. 2, pp. 1057–1060.
- Smith, J. P., Johnson, B. D., and Burdisso, R. A. (1999). “A broadband passive-active sound absorption system,” *J. Acoust. Soc. Am.* **106**(5), 2646–2652.
- Thomson, C. J. (2012). “Research Note: Internal/external seismic source wavefield separation and cancellation,” *Geophys. Prospect.* **60**(3), 581–587.
- Ting, L., and Miksis, M. (1986). “Exact boundary conditions for scattering problems,” *J. Acoust. Soc. Am.* **80**(6), 1825–1827.
- van Manen, D.-J., Robertsson, J. O. A., and Curtis, A. (2007). “Exact wave field simulation for finite-volume scattering problems,” *J. Acoust. Soc. Am.* **122**(4), EL115–EL121.
- van Manen, D.-J., Vasmel, M., Greenhalgh, S., and Robertsson, J. O. A. (2015). “Broadband cloaking and holography with exact boundary conditions,” *J. Acoust. Soc. Am.* **137**(6), EL415–EL421.
- Vasmel, M., Robertsson, J. O. A., van Manen, D.-J., and Curtis, A. (2013). “Immersive experimentation in a wave propagation laboratory,” *J. Acoust. Soc. Am.* **134**(6), EL492–EL498.
- Vasquez, F. G., Milton, G. W., and Onofrei, D. (2011). “Exterior cloaking with active sources in two dimensional acoustics,” *Wave Motion* **48**(6), 515–524.
- Wang, Y. (2015). “Frequencies of the Ricker wavelet,” *Geophysics* **80**(2), A31–A37.
- Wapenaar, C. P. A. (1993). “Kirchhoff-Helmholtz downward extrapolation in a layered medium with curved interfaces,” *Geophys. J. Int.* **115**(2), 445–455.
- Willard, E. (2019). “Acoustic transducer design for active reflection cancellation in a finite volume wave propagation laboratory,” Master’s thesis, The University of Texas at Austin, Austin, TX.
- Willard, E., Haberman, M. R., van Manen, D.-J., Robertsson, J. O., Becker, T. S., and Börsing, N. (2018). “Acoustic transducer design for active reflection cancellation in a finite volume wave propagation laboratory,” *J. Acoust. Soc. Am.* **144**(3), 1759–1759.
- Williams, J. E. F. (1984). “Review Lecture—Anti-sound,” *Proc. R. Soc. London. A. Math. Phys. Sci.* **395**(1808), 63–88.
- Wilson, O. (1988). *Introduction to Theory and Design of Sonar Transducers* (Peninsula Publishing, New York).
- Wilson, O. B., and McMahon, G. W. (1987). “An introduction to the theory and design of sonar transducers,” *J. Acoust. Soc. Am.* **81**(6), 1999.
- Woollett, R. S., and Finch, R. D. (1990). “The flexural bar transducer,” *J. Acoust. Soc. Am.* **87**(3), 1378.
- Yilmaz, O. (2001). *Seismic Data Analysis* (Society of Exploration Geophysicists, Tulsa).